Dense Point Cloud Quality Factor (DPQF) as A Proxy for Accuracy Assessment of Image-based 3D Reconstruction

Farid Javadnejad[1,*], Richard K. Slocum[1], Daniel T. Gillins[2], Michael J. Oslen[1], Christopher E. Parrish[1]

Abstract

Small unmanned aircraft systems (UAS) carrying consumer-grade nonmetric cameras are increasingly being used to generate high-resolution 3D geospatial data. The photogrammetry and computer vision techniques Structure from Motion (SfM) and Multi-View-Stereopsis (MVS) can recover structure from a set of overlapping, un-oriented, and uncalibrated images. Those techniques have been widely adopted for UAS-based photogrammetry. It is possible to generate accurate reconstructions of sparse points using mathematically robust bundle adjustment (BA) procedures together with accurate surveying control data. However, MVS, which recovers the dense geometry by matching and expanding between sparse points through enforcing epipolar geometry constraints based on camera exterior orientation (EO) parameters from the initial BA is

[1] School of Civil and Construction Engineering, Oregon State University, 101 Kearney Hall, 1491 SW Campus Way, Corvallis, OR 97331, USA
[2] National Geodetic Survey, National Oceanic and Atmospheric Administration, 1315 East-West Highway, Silver Spring, MD 20910, USA
[*] *Corresponding author: fjnejad@lifetime.oregonstate.edu*

prone to additional error. It has been shown that factors such as image overlap, number of ground control points (GCPs), scene complexities, camera standoff distances, lighting condition, lack of texture in the scene, shadowing, etc. may introduce random noise or smoothing effects that can locally degrade the accuracy of the dense point cloud. This paper introduces dense point cloud quality factors (DPQF) as proxy indicators for assessing the accuracy of SfM-MVS dense point clouds. Simulated and empirical experiments are used to assess the accuracy of image-based 3D reconstructed models under various data collection and site condition scenarios. The spatial correlation between the DPQFs and the reconstruction error is investigated and interpreted for multiple experiments. The results of this study show that the DPQF can be a helpful additional field of information for 3D point clouds. The advantage of the DPQFs is that the factors can be defined solely based on the inputs and results of the SfM-MVS processing without prior knowledge about the error. Visualization of the factors may provide a proxy indicator for accuracy, while the error estimation for dense point clouds is more challenging than error propagation computations in BA. Further comprehensive experiments and studies are required to draw firm conclusions for a better application on DPQFs for accuracy assessment. However, the use of DPQFs that have physical definitions enables the development of more tangible intuitions regarding factors, which influence 3D reconstruction accuracy.

1. Introduction

High-resolution three dimensional (3D) data is essential for detailed spatial interpretation and analysis in many geomatics applications (Abellan et al. 2016; Che and Olsen 2017; Javadnejad 2013; Javadnejad et al. 2017b; Mahmoudabadi et al. 2016; McCaffrey et al. 2005; O'Banion 2017;

Olsen et al. 2015; Omasa et al. 2006; Sohn and Dowman 2007; Wood et al. 2017). Increasingly, modern photogrammetry utilizing consumer-grade nonmetric cameras mostly mounted on the small unmanned aircraft systems (UAS), is being used to generate the high-resolution 3D data. Because of the widespread availability, low maintenance cost, ease of operation, low altitude maneuvering capability, and flexible and frequent data collection, UAS-based photogrammetry is changing the surveying and mapping research and industry (Colomina and Molina 2014; Pajares 2015). UAS-based photogrammetry has been tested in different environments, and its advantages and disadvantages have been explored (Faraji et al. 2016; Gao et al. 2017; Griffin 2014; Javadnejad 2018; O'Banion et al. 2018; Shi et al. 2016; Wood et al. 2017). There are a number of open source programs such as *VisualSfM* (Wu 2011) and Bundler (Snavely et al. 2006), as well as commercial packages such as *PhotoScan*, now named *Metashape* (Agisoft 2018) and *Pix4DMapper* (Pix4D 2018) that are commonly used for processing the imagery collected from UAS platform to generate high-resolution mapping products such as 3D point clouds, mesh surfaces, digital terrain models (DTMs), and orthoimages.

The photogrammetry from the nonmetric digital cameras includes using structure from motion (SfM) and multi-view stereopsis (MVS) techniques that recover structure from a set of overlapping un-oriented and uncalibrated images, and generate 3D dense point clouds (Eltner et al. 2016; Furukawa and Ponce 2010; Seitz et al. 2006). The general steps for SfM photogrammetry are shown in Figure 1. The processing starts with automatic extraction of key features from the raw imagery (Harris and Stephens 1988; Lowe 1999; Snavely et al. 2008; Szeliski 2010; Tomasi and Kanade 1992). Then the extracted features are described in multidimensional descriptors, e.g., SIFT (Lowe 1999, 2004). The procedure is followed by matching the features (Snavely et al. 2008; Szeliski 2010) and outlier rejection (Crandall et al. 2013; Fischler and Bolles 1981). Later, the bundle adjustment (BA) (Heung-Yeung Shum et al. 1999; Triggs et al. 1999) simultaneously solves for the intrinsic orientation (IO) and extrinsic orientation (EO) parameters of the cameras and to generate a sparse point cloud (Crandall et al. 2013; Snavely et al. 2008; Szeliski 2010). The reconstructed model is transformed to a real-world coordinate system using either known ground control points (GCPs) coordinates or via UAS-based GNSS camera pose estimations (Javadnejad and Gillins 2016). In addition to georeferencing the SfM point clouds, use of GCPs can also improve the accuracy of the model during the second step of the BA by performing a nonlinear optimization on the estimation of sparse points coordinates, and the camera IO and EO parameters. In this step, the camera parameters and the constructed geometry are reoptimized by minimizing the reprojection error of feature matches in the form of a sparse point cloud after importing the GCPs (Heung-Yeung Shum et al. 1999).

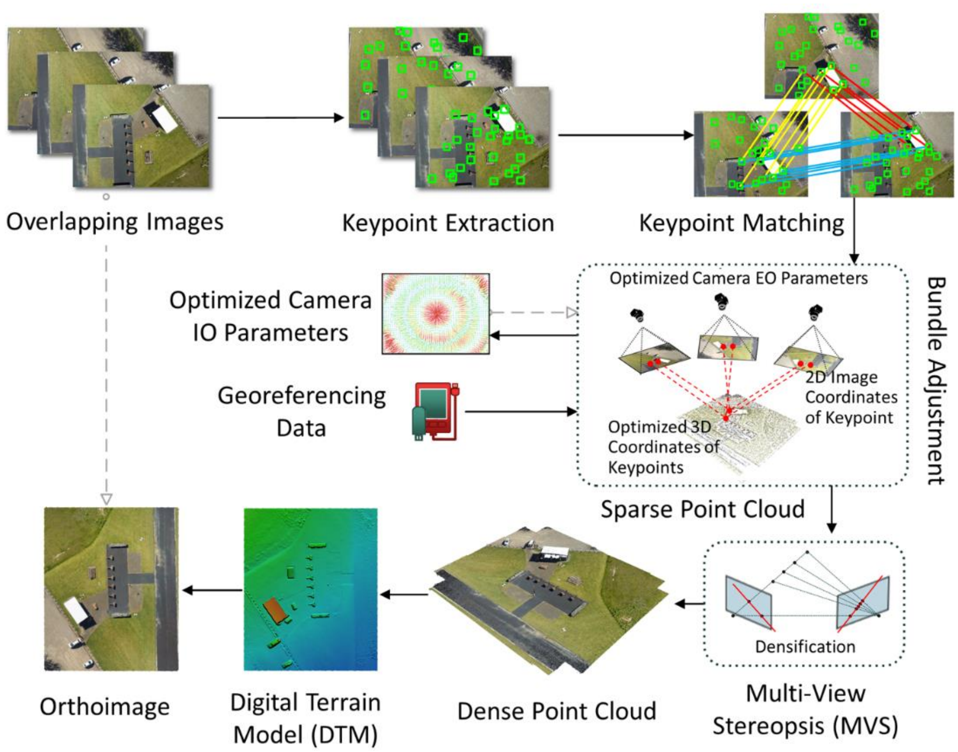

Figure 1: Steps of SfM-MVS processing (Javadnejad 2018)

The sparse point cloud is ordinarily complemented with a densification step through MVS processing, which generates a depth map for pixels of the image based on photo-consistency in an oriented block obtained from bundle adjustment (Furukawa and Ponce 2010; Remondino et al. 2014; Snavely et al. 2008). Together with accurate input data, it is possible to produce an accurate reconstruction of sparse points using the mathematically robust BA procedure. On the other hand, MVS, which recovers the densified point cloud by matching and expanding between sparse points may yield results with different and inconsistent accuracies. MVS works by enforcing epipolar geometry constraints obtained from BA solution, and later filtering the outliers (Furukawa and Ponce 2010). MVS algorithms are continuously being improved regarding accuracy and completeness, identifying and recognizing the sources reconstruction error, and estimating the accuracy and reliability are still ongoing research topics (Furukawa and Ponce 2010; Yao et al. 2014; Zhu et al. 2015). A good number of research studies have investigated the applicability of the technique for a variety of mapping instances; also more researches are being carried out on the accuracy of SfM-MVS products (e.g., Javadnejad (2018) and references therein).

Uncertainty in image-based 3D reconstruction is function of various input data factors and processing parameters such as the quality of the input image, accuracy, number and distribution of ground control points (GCPs), the accuracy of IO and EO parameters, certainty in feature detection and matching in overlapping images or even choice of reconstruction technique (Hofsetz et al. 2004; Seitz et al. 2006). The accuracy of SfM-MVS can be defined as the closeness of the empirical measurements to a reference ground truth, such as a comparison between SfM-MVS and a lidar point cloud or total station and/or GNSS measurements at checkpoints (CPs). Unlike GCPs, the CPs are not used for georeferencing or sparse point cloud optimizing; however, the known values of the CPs are compared to the coordinate measurements of the same points in the 3D geometry and is reported for accuracy assessment purposes (Javadnejad and Gillins 2016). Besides empirical comparisons, Slocum and Parrish (2017) proposed a workflow, which uses a simulated graphics environment for generating virtual UAS surveys to overcome challenges of empirical surveys such as the time and cost of data collecting campaigns. This approach incorporates the systematization of a reliable ground truth reference, and also leverages the isolation of environmental factors that contribute to error budget in SfM-MVS models while it enables investigation of the impact of individual parameters (Slocum and Parrish 2017).

In mapping and surveying applications, it has been found that the accuracy of SfM-MVS sparse and dense point clouds is influenced by many factors such as image overlap, number of images, lens distortion model, number of ground control points (GCPs), geometry of GCP distribution, geometry of camera distribution, accuracy of GCP or camera positions, image resolution, blurriness of imagery, noise of imagery, lighting condition, shadow effect, scene complexities, standoff distances, image-matching performance, image texture, presence of dense vegetation, moving objects in the scene, and user errors in selecting the image coordinates of GCPs (Agüera-Vega et al. 2017; Carbonneau and Dietrich 2017; Clapuyt et al. 2016; Dandois et al. 2015; Eltner et al. 2016; Fonstad et al. 2013; Harwin et al. 2015; Harwin and Lucieer 2012; James et al. 2017a; b; Javadnejad et al. 2017a; Smith and Vericat 2015; Tonkin and Midgley 2016; Westoby et al. 2012).

This paper introduces seven different factors, named dense point cloud quality factors (DPQFs), as proxy indicators for the accuracy of image-based reconstruction. The factors include (1) distribution of the keypoint features resulting from the BA, (2) distribution of GCPs, (3) scene geometry, (4) camera stand-off distances, (5) number of images, (6) brightness index, and (7) darkness index. Although other studies presented the impact of some of these factors, this study investigates the correlation between these factors to outline the importance of each factor for different scenarios holistically. This research study investigates the correlation of the DPQF with reconstruction error for sets of simulated and empirical data with multiple scenarios. The work is also meant to help surveyors with planning the best data collection strategies for UAS/SfM photogrammetry projects to minimize error by providing definition of indices that can be optimized during data collection for an improved accuracy. Also, it is within the scope of this paper to supplement the point cloud with additional quality indices that can be helpful for visualization and identifying points that are prone to inaccurate reconstruction, and weighting for mesh generation. An advantage of the DPQFs is that the factors can be defined solely based on the inputs and results of SfM-MVS processing. They can provide a proxy indicator for dense point clouds quality, while the estimation of error for dense point cloud is more challenging than the error propagation estimation in BA.

2. Materials and methods

This paper presents a simulated experiment based on the simUAS approach (Slocum and Parrish 2017), where the different scenarios for a scene are created, as well as an empirical case study exploring the use of both lidar and UAS for surveying a construction site. Digital photographs acquired from both datasets are post-processed using SfM techniques to produce a high-resolution point cloud. The error is defined as distance to the control data. The ground truth for the simulated data is perfectly known and can be exported as a mesh model from the simulation environment, and the ground truth for the empirical data is the lidar. The resultant dense point clouds and error indices are used to estimate the DPQF value, which is later investigated for statistical correlation between all the factors and the error index to identify impact and importance of each factor. Figure 2 shows the approach used for estimating DPQF for both the simulated and empirical datasets.

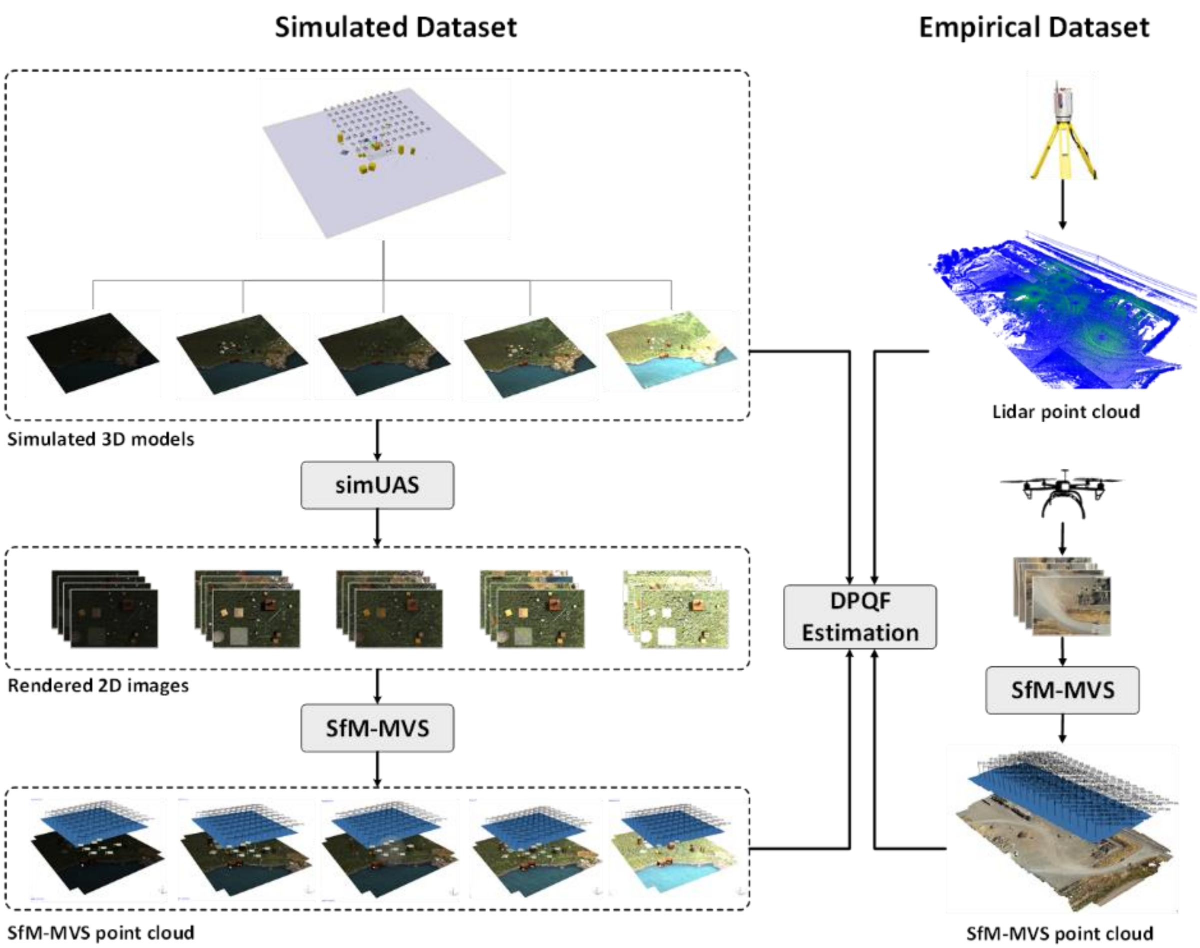

Figure 2: Workflow for data preparation of simulated and empirical datasets, and DPQF estimation

2.1. Datasets

- *Computer graphics simulation*

The simulations were performed using the Blender® software (Blender 2017), a free open-source 3D computer graphics software, following the simUAS approach (Slocum and Parrish

2017). The simulated scene is a site that consists of a flat plane surface, 11 boxes, 7 horizontal cylinders representing pipes, 6 vertical cylinders, 3 spheres, 5 pyramids, 2 cones and 3 icosphere of varying sizes (Figure 3). The objects were textured using a variety of texture images acquired from freely available online datasets such as brick, concrete, metal, wood, gravel, asphalt, and soil (Figure 3c). Two different scenes named “A” and “B’ were generated by applying different texture to the ground plane. In scene A, the plane was textured using a 9620 by 9620 pixels image that was generated by tiling 6 high-resolution aerial images with 10cm pixel resolution (0.1m GSD) acquired over the Invercargill City in New Zealand that includes forest as well as industrial, and water textures (Figure 3a) (LINZ 2016). For the scene B, a 50 by 50-pixel Gaussian Smoothing filter with Sigma 0.5 was applied to the aerial image. Then it was overlaid with a transparent random noise image (Figure 3b). In both scenes, 14 black and white iron cross targets, similar to the one shown in Figure 3, were placed in the scene.

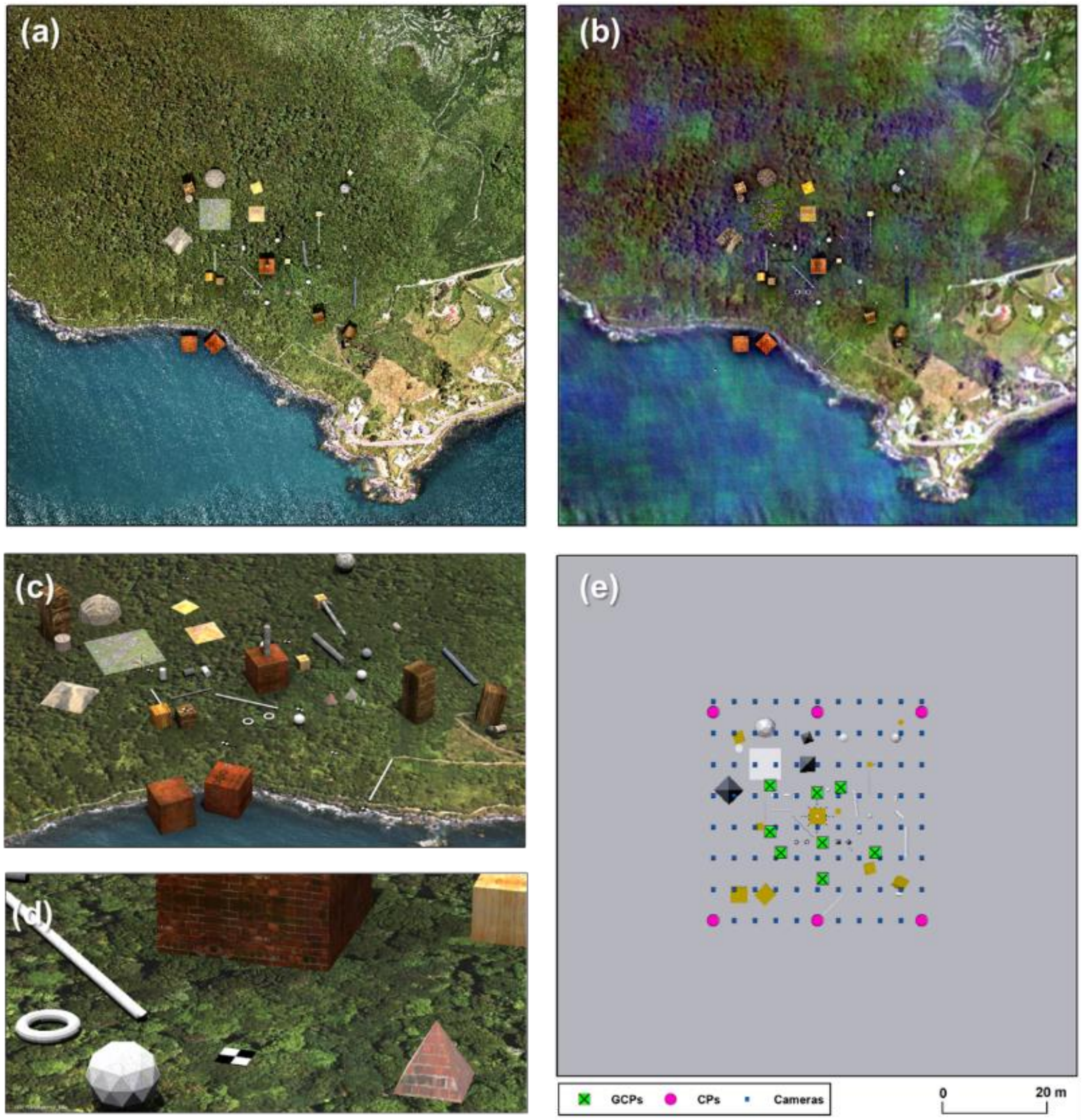

Figure 3: (a) overview of simulated scene A, (b) overview of simulated scene B, (c) different objects placed in the simulated scene with surface textures, (d) close-up view of textured objects as well as a black and white GCP on the scene, and (e) the location of objects, GCPs, CPs, and the position of cameras

Both scenes were illuminated with 5 different sun and ambient light intensities to create variation in lighting and shadows. Table 1 shows the different lighting conditions in the simulation. Scenarios 1 and 5 are the darkest and brightest allowing the existence of underexposed and overexposed object at the scene. Underexposure and overexposure, occur when camera sensor does not record enough details in the darkest and rightest part of the images, respectively. Scenario 2 is brighter than the first scenario with stronger sunlight and lower ambient light creating strong shadow areas. The higher ambient light intensity in scenario 3 minimizes the intensity of shadow, and scenario 4 has high sun and ambient light intensity creating appropriate contrast on textures (proper exposure). The impact of the different light on the accuracy of reconstruction is later studied.

Table 1: Sunlight and ambient light settings used for scenarios 1 to 5 of A and B, and the resultant simulation for scenarios A1 to A5. The intensity values are in the range between 0.0 to 10.0 with low values the sky has no sun, and with high values the sky only has sun.

Scenario	1	2	3	4	5
Sun Light	0.2	0.9	0.1	0.9	2.5
Ambient Light	0.2	0.1	0.9	0.9	2.0
Output	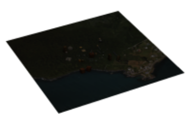	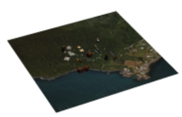			

To simulate the UAS-based data collection, 88 cameras were positioned across the area including the simulated objects (Figure 3). The camera was set to mimic the Sony A5000 with 16 mm focal length and output image sizes of 5456 by 3632 pixels. The simulated cameras were placed at 20 m AGL altitude and the flight lines with respect to the height and width of the images to keep 80 % of side and forward overlap. For the scenes A and B with 5 different lighting scenarios, images were rendered at the given cameras locations using the Blender® Internal Render Engine and the resulted images were post-processed using simUAS in MATLAB® (MathWorks 2017) to add non-linear Brown’s lens distortion to the images. This approach has been described in details by Slocum and Parrish (2017) for interested readers. Overall, it took about

4 hours to perform both the image rendering in Blender and the post-processing in MATLAB for each experiment. In total 10 experiments were simulated with A and B scenes, five different scenarios each.

- *Empirical case study*

The study area for the empirical assessment is a storage yard utilized by Linn County in the State of Oregon to store gravel, asphalt grindings, debris, spare concrete bridge parts, and piping material. It is located approximately 5 km northwest of the City of Lebanon (Figure 4). The data for this site consists of terrestrial lidar data as well as the aerial imagery collected from a UAS. Prior to data collection, 18 aerial targets (Figure 5a), and 12 boxes with patterned targets (Figure 5b) were distributed throughout the scene. The aerial targets, approximately 1 square meter in size, were nailed to the ground to ensure stability throughout the flight (Figure 5a). In addition, 38 color cross markings (such as the markings in Figure 10.f) were placed at two ends and the center of pipe sections to check the accuracy of SfM results. Figure 6 shows the layout of the control network. Repetitive, 3-minute observations were acquired on all aerial targets using a Leica GS14 survey-grade GNSS receiver obtaining real-time kinematic corrections from the Oregon Real-Time GNSS Network (ORGN). The ORGN is a statewide real-time network managed by the Oregon Department of Transportation (ODOT 2017). Also, all the aerial targets, markings and box targets were surveyed using radial traversing methods with a Leica TS15 Total Station. It took 3.5 hours in total to complete the ground surveying campaign to establish coordinates for the targets and markings. The approach for a similar ground control network survey has been described in more detail by Javadnejad and Gillins (2016) for interested readers.

Figure 4: Langmack storage facility (image data ©2017 Google Earth Landsat/Copernicus Data SIO, NOAA, U.S. Navy, NGA, GEBCO and ©2017 Google Maps)

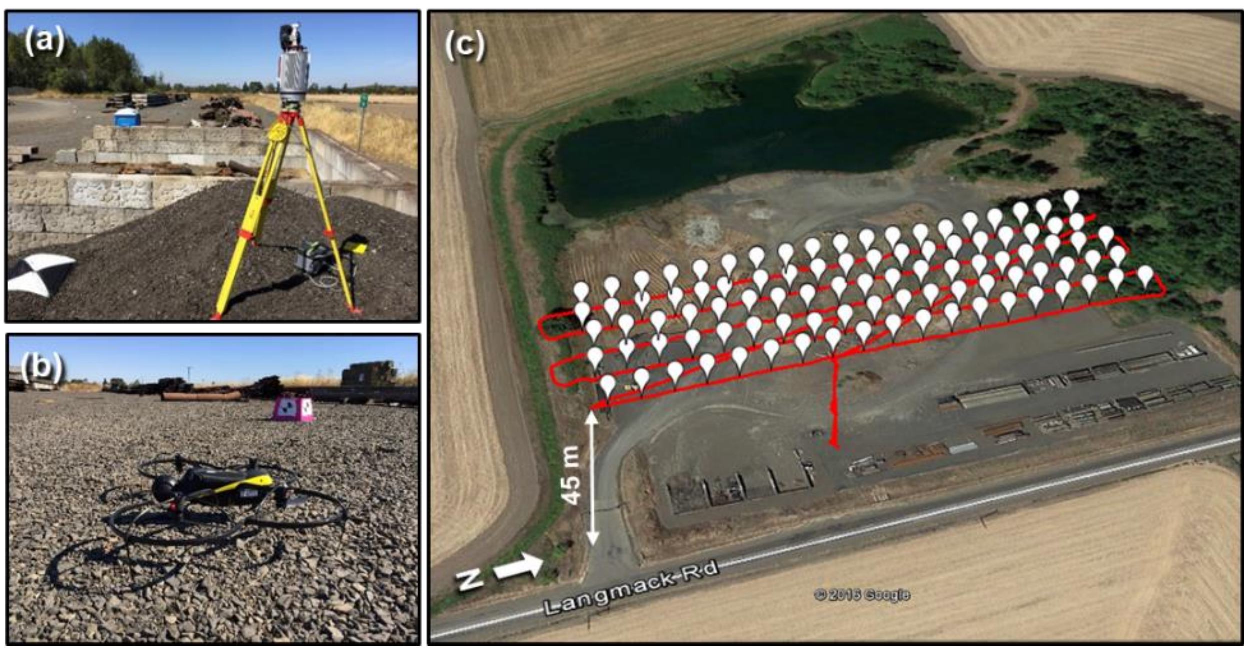

Figure 5: (a) The Riegl VZ400 and a nearby GCP, (b) the Albris and a target box, and (c) the flight pattern (image data Landsat/Copernicus ©2016 Google Earth)

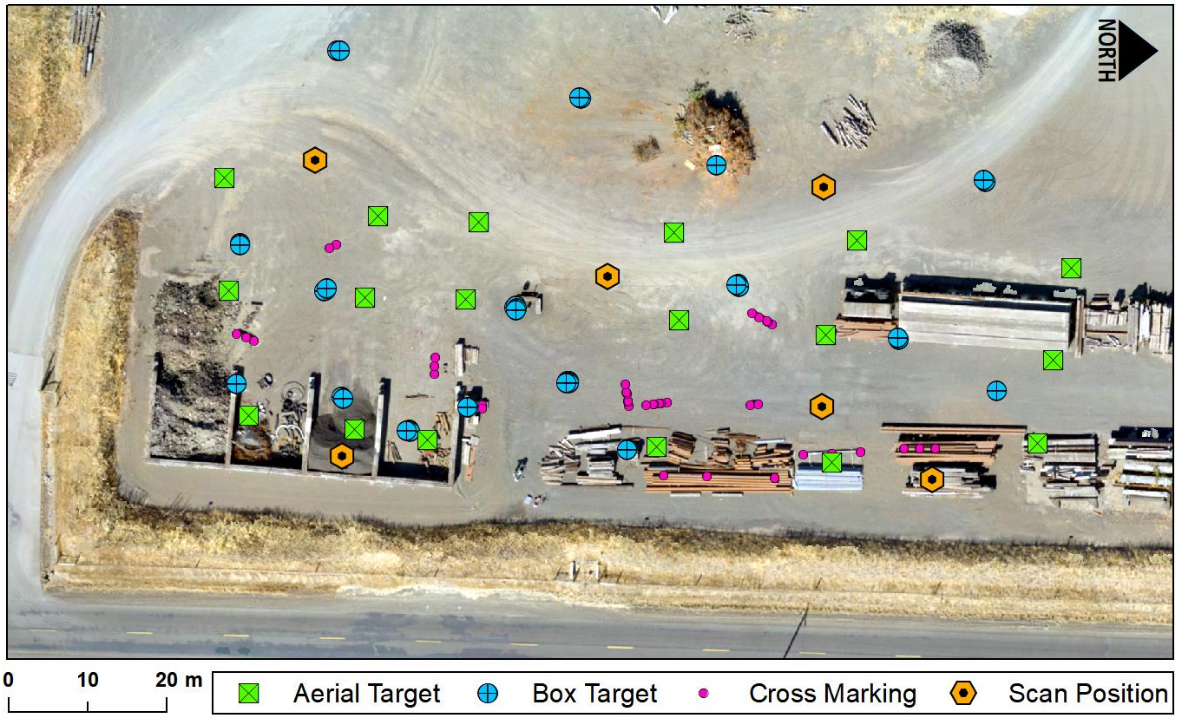

Figure 6: Location of the established aerial targets, cross markings, box targets, and scan positions

The box targets (Figure 5b) were placed strategically to be seen by the majority of the scans throughout the site by distributing the targets across the study area in a 15 to 20 m grid pattern (Figure 6). The lidar data of the site was collected via 6 separate scans using a Riegl VZ-400 scanner (Figure 5a). Each scan was 7 minutes in duration. In total, it took 1.5 hours for the entire scan data collection, including setup and data capture times. The SenseFly Albris (formerly known as the eXom) (Figure 5b) was used for collecting the aerial images. The flights were completed on August 17, 2016, under the Oregon State University (OSU) Certificate of Authorization (COA) for public UAS operations. The Albris has an integrated GNSS receiver and inertial navigation system that allows the craft to fly to predefined mission waypoints. The visible sensor on this platform is a Nokia camera with 10.01 by 7.51 mm sized sensor and 7.9 mm focal length, producing 7152 by 5368 pixel images. The flights were performed such that nadir photographs were systematically collected with 80% side and 80% forward overlap at 45 m above the ground level, resulting in a ground sampling distance (GSD) of 8 mm per pixel. The camera was triggered with automatic focus and exposure modes by the onboard autopilot system when the aircraft reached the preplanned flight mission waypoints (Figure 5c). In total, 95 images were collected during an 11-minute flight.

2.2. Point cloud generation

- *Simulated data*

The resulted imagery from simulations and the actual UAS operation at the Langmack site were processed using the commercial software *PhotoScan Pro* 1.4 (Agisoft 2018). *PhotoScan* can generate point clouds, textured polygonal models, georeferenced orthoimages and DEMs. In *PhotoScan*, the georeferencing is performed by identifying the GCPs in the photographs, inserting the coordinates and their standard deviation values, and/or by providing the location and orientation of the cameras. The exact position of the cameras, the camera calibration models, 3D coordinate and pixel coordinates of the GCPs and CPs of simulated scenes were imported to *PhotoScan*. The statistics of SfM processing are shown in Table 2. The final dense point clouds were processed using “medium quality” and “aggressive-depth filtering” settings. The total processing time was 15 minutes for each scenario.

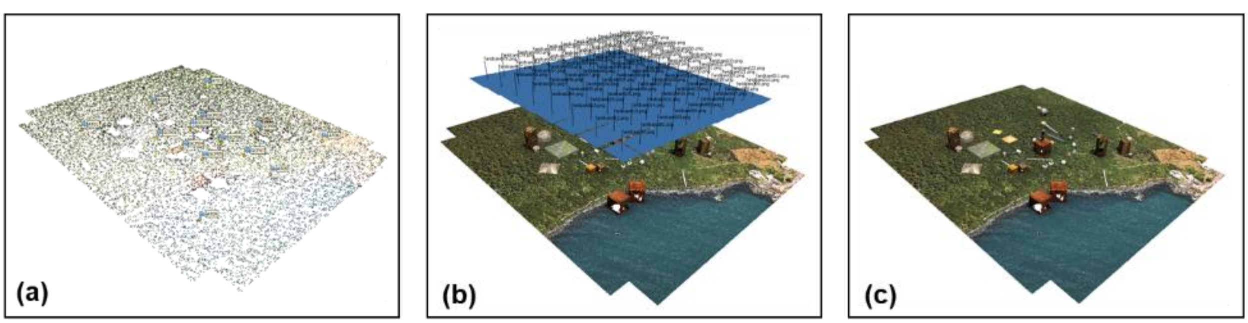

Figure 7: (a) Resultant sparse point cloud, (b) dense point clouds with the cameras locations and orientations, and (c) dense point clouds reconstructed for simulation A3

Table 2: General information of SfM-MVS processing and the resulted point cloud for scenarios of simulation scenes A and B

Simulation	Attribute	1	2	3	4	5
A	No of points (Sparse)	25.8×10^3	25.5×10^3	25.1×10^3	24.8×10^3	25.0×10^3
	RMSEGCP (mm)	0.05	0.03	0.02	0. 05	0.06
	RMSECP (mm)	2.0	1.9	1.9	1.8	1.8
	No of points (Dense)	9.5×10^6	9.7×10^6	9.4×10^6	9.4×10^6	9.2×10^6
B	No of points (Sparse)	28.9×10^3	26.7×10^3	26.0×10^3	25.6×10^3	25.4×10^3
	RMSEGCP (mm)	0.09	0.03	0.04	0.06	0.03
	RMSECP (mm)	2.0	2.0	1.8	1.9	1.9
	No of points (Dense)	9.9×10^6	10.2×10^6	9.6×10^6	10.2×10^6	9.2×10^6

- *Empirical data*

For the Langmack dataset, the coordinates of the targets and markings were determined by performing a least square adjustment (LSA) on the network of Total Station and GNSS observations within Star*NET 8.0 using the approach described by Javadnejad and Gillins (2016). The adjustment resulted in an estimated horizontal and vertical root mean square error (RMSE) of 1.97 mm and 2.8 mm, respectively, for the ground control network coordinates. The resultant coordinates were used to post-process the 95 aerial images collected during the UAS flights in *PhotoScan*. The data was reprocessed for five scenarios with selecting 4, 6, 8, 12 and 18 GCPs from aerial targets and using the rest of aerial targets and/or markings and CPs. The total error on GCPs and CPs is reported in Table 3. The final dense point cloud was processed using “high quality” and “mild-depth filtering” settings. The total processing time for each scenario, was 1 hour to generate a dense point cloud.

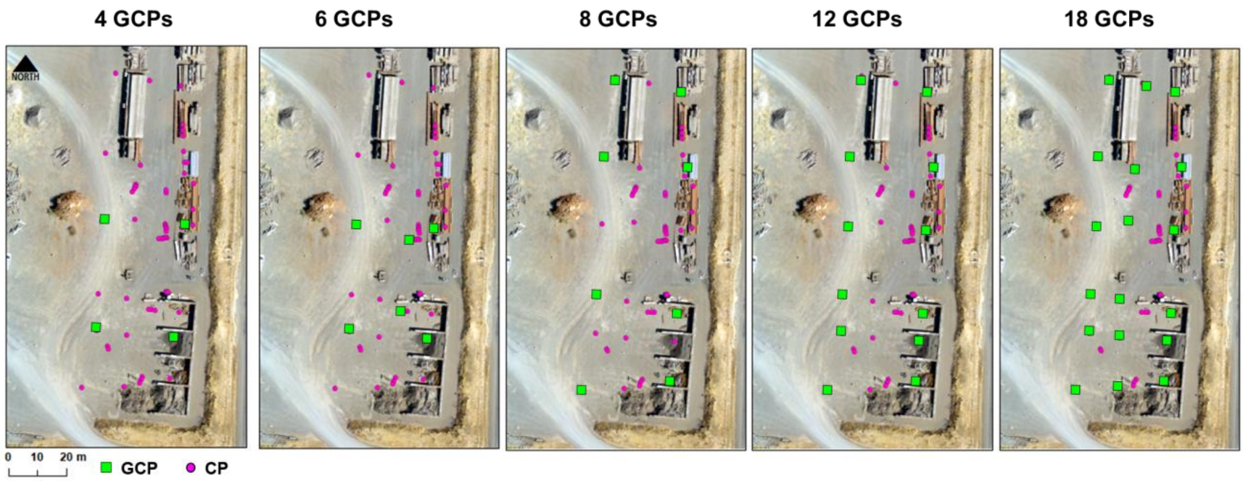

Figure 8: The overview of GCPs selection for scenarios of empirical dataset

Table 3: General information of SfM-MVS processing and the resulted point cloud for empirical data

No GCPs	4	6	8	12	18
No of CPs	52	50	48	44	38
RMSEGCP (m)	0.004	0.009	0.011	0.012	0.013
RMSECP (m)	0.058	0.028	0.024	0.016	0.016
No of points (sparse)	5.5×10^3	5.5×10^3	5.5×10^3	5.5×10^3	5.5×10^3
No of points (dense)	84.6×10^6	84.6×10^6	84.6×10^6	84.4×10^6	84.4×10^6

The resultant coordinates from LSA were also used to register the lidar dataset to the same coordinates as the SfM data. All 6 scans were co-registered by constraining the clouds to the extracted targets and cloud-to-cloud registration in *Cyclone* 9.1 (Leica Geosystems 2016). The registration resulted in a 3D RMSE of 1.4 cm and 1.5 cm for target only, and target and cloud-to-cloud (C2C) constraints, respectively. The composite point cloud of all scans contained 101 million points within the study area. The lidar point clouds were resampled at minimum space between points to be 2 cm to increase the processing speed; then the lidar point cloud was cropped to the area with existing SfM-MVS dense point clouds to avoid miscalculation of Lc2c for points out of the SfM model. The resampled and cropped point clouds included about 14.2 million points (Table 4).

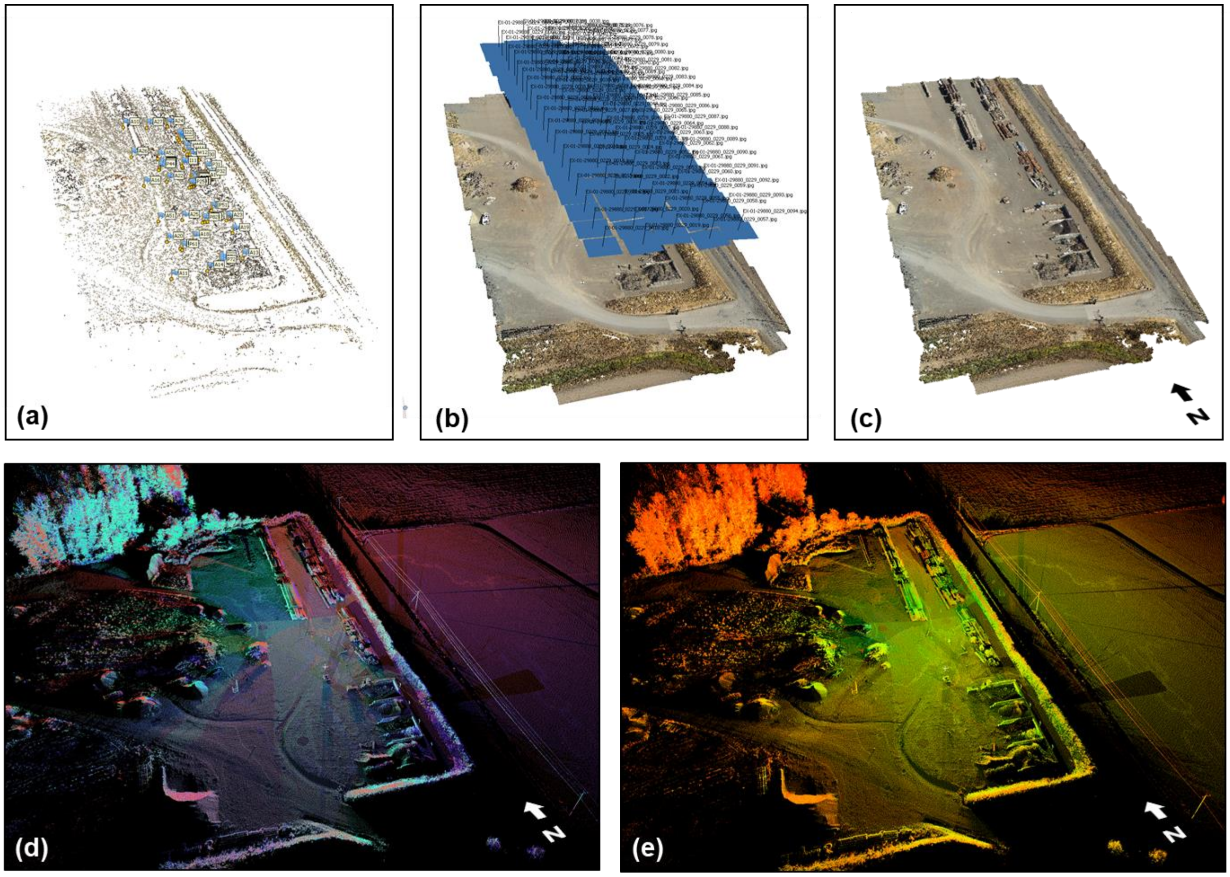

Figure 9: (a) Resultant sparse point clouds, (b) dense point clouds and cameras location and orientation, and (c) dense point clouds reconstructed for simulation A3, (d) lidar point clouds colored differently for each scanner, and (e) intensity-colored lidar point clouds

Table 4. General information of lidar for empirical dataset

No of scans	No of targets	RMSE (targets)	RMSE (target and C2C)	No of points
6	21	1.4 cm	1.5 cm	101.1×10^6

2.3. Dense point cloud quality factors (DPQF)

The overview of this approach is schematically shown in Figure 2. The following section describes the DPQF and how they are calculated. The estimated quality indices are attributed as additional fields together with the traditional *X*, *Y*, *Z*, and color values of the ground truth point cloud. For empirical data, the lidar was used as the ground truth model, and for simulation data, the simulated 3D geometry was exported as wavefront obj file, and then the obj model was resampled with 10 million points in the open source software CloudCompare (Girardeau-Montaut 2017).

- *3D error* (e)

The error index is defined as a comparison between the ground truth model and the SfM-MVS dense point cloud. In this study, the error is calculated as the absolute 3D cloud-to-cloud distance (LC2C) of each point in ground truth data from the closest point in the SfM point cloud. Lague et al. (2013) recommended to for interested readers for more information about approaches on 3D cloud-to-cloud comparison.

- *Distance to keypoint features* (d_{kp})

The LC2C for each ground truth point was calculated from the closest keypoint feature in CloudCompare.

- *Distance to GCP* (d_{gcp})

The locations of the GCPs used for georeferencing the SfM models were imported to CloudCompare, and the LC2C between the ground truth point cloud and GCPs were calculated.

- *Scene geometry* (α)

The scene geometry and the data collection pattern can be described by the angle of incidence between the surface normal at the point P and the line from the camera center C to the point using Eq. 1:

$$\alpha_{\mathrm{inc}} = \tan^{-1}\left(\frac{\left\|\vec{N}_{\mathrm{P}} \times \vec{u}_{\mathrm{CP}}\right\|}{\vec{N}_{\mathrm{P}} \cdot \vec{u}_{\mathrm{CP}}}\right) \tag{1}$$

where $\overrightarrow{\boldsymbol{N}}_{\mathrm{P}}$ is the surface normal vector at the point and $\vec{u}_{\mathrm{PC}}$ is the unit vector between the point and the camera that is calculated using their position vector in Eq. 2:

$$\vec{u}_{\mathrm{CP}} = \frac{1}{\|\vec{r}_{\mathrm{P}} - \vec{r}_{\mathrm{C}}\|}(\vec{r}_{\mathrm{P}} - \vec{r}_{\mathrm{C}}) \tag{2}$$

The point normal vectors were estimated by fitting quadratic surfaces to the neighboring points (OuYang and Feng 2005) in $+z$ orientation, and the camera positions were obtained from the estimated camera EO from the SfM solution. The average of all angle of incidence between the point and all the cameras that point is attributed to the point. If all the cameras are pointing to a particular direction for example, in vertical photogrammetry, it is possible to use the $-z$ unit vector $(0,0,-1)$ and just calculate the angle of the surface (α_{sur}) instead of the angle of incidence.

- *Camera stand-off distances* (d_c)

The stand-off distances between the point P in ground truth point cloud and the camera are calculated using their 3D coordinates (Eq. 3), then the average distance between the point and all cameras which are attributed to the point.

$$d_{\mathrm{c}} = \|\vec{r}_{\mathrm{C}} - \vec{r}_{\mathrm{P}}\| \tag{3}$$

- *Number of images* (n_{img})

Using the IO and EO parameters obtained from SfM solution as well as the real-world coordinate transformation parameters, it is possible to back calculate the 2D pixel coordinates of every 3D point in the scene. For each point, if the 2D coordinates are located in the image, the counter is augmented by 1, and the final counter value of the number of images is attributed to the point in the cloud. This approach lacks the ability to deal with occlusions; however, on approach to deal with the problem is by considering the angle of incidences. The point is considered to be seen in the image if the angle of incidence is less than 90 degrees. This criterion filter the points that are on the surfaces that do not face the camera, while their pixel coordinates are within the image plane. Future developments can incorporate more advanced ray tracking analysis in the number of image calculations. For this study, there was minimal occlusion in the scene. Hence the effect of those occlusions on the DPQFs is determined to be negligible.

- *Brightness (I_b) and darkness (I_d)indices*

RGB color values were used to define the brightness and darkness factors. The RGB values were converted to a normalized grayscale scale intensity values between -1 and 1 (Eq. 4) (Anderson et al. 1996), then the brightness and darkness indices were calculated for each point using Eq. 5.

$$\tilde{I}_{\mathrm{gray}} = \frac{2 \times (0.2126 \times \mathrm{R} + 0.7152 \times \mathrm{G} + 0.0722 \times B)}{255} - 1 \tag{4}$$

$$\begin{cases} I_{\mathrm{b}} = \tilde{I}_{\mathrm{gray}},\ I_{\mathrm{d}} = 0 & \tilde{I}_{\mathrm{gray}} > 0 \\ I_{\mathrm{d}} = \tilde{I}_{\mathrm{gray}},\ I_{\mathrm{b}} = 0 & \tilde{I}_{\mathrm{gray}} < 0 \end{cases} \tag{5}$$

3. Results and discussion

Figure 10 shows the ground truth models (a, e), SfM-MVS dense point clouds (b and f), and the calculated 3D error for sections of the scene A3 of simulated (c) and the empirical datasets (g). Also, a profile view of a box in the simulated data (d) and a pipe in the empirical data (h) are shown, and the LC2C calculations are schematically illustrated. Figure 11 and Figure 12 shows the maps of error and the DPQF indices including, keypoint features distribution d_{kp}, GCP distribution d_{gcp}, scene geometry α_{sur}, camera stand-off distances d_{c}, image coverage n_{img}, brightness index I_b and darkness index I_d for a simulated scene (A3 scenario) and an empirical dataset (6 GCP scenario).

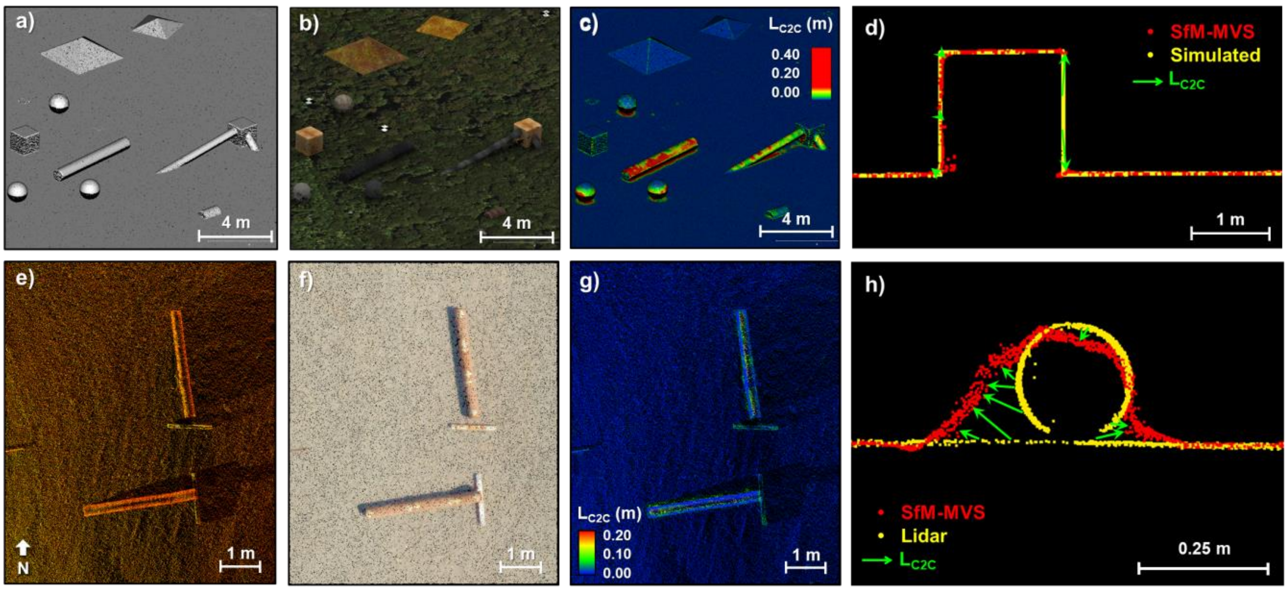

Figure 10: (a) ground truth model for a section of scenario A3, (b) SfM-MVS dense point cloud for scenario A3, (c) 3D error vizlauzaiotn for scenario A3, (d) a crosssection of reconstructed and ground truth point clouds and schematic error calcaution for scneario A3, (e) lidar point cloud for a section of Langmack dataset with 18 GCPs, (f) SfM-MVS dense point cloud for a section of Langmack dataset with 18 GCPs, (g) 3D error vizlauzaiotn for a section of Langmack dataset with 18 GCPs, (h) a crosssection of reconstructed and ground truth point clouds and schematic error calcaution for a section of Langmack dataset with 18 GCPs

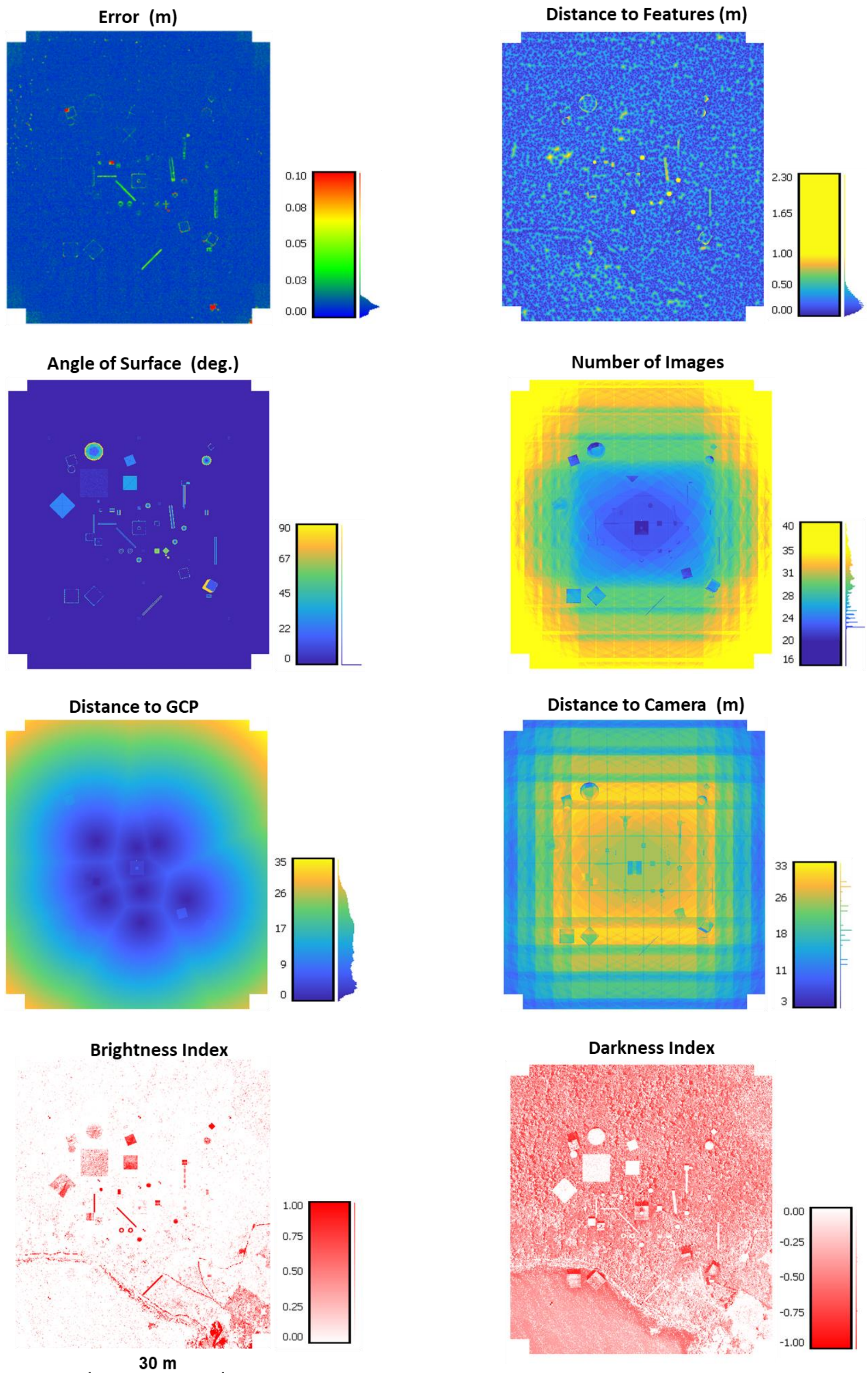

380

381 **Figure 11: DPQFs for scenario A4 of simulated dataset**

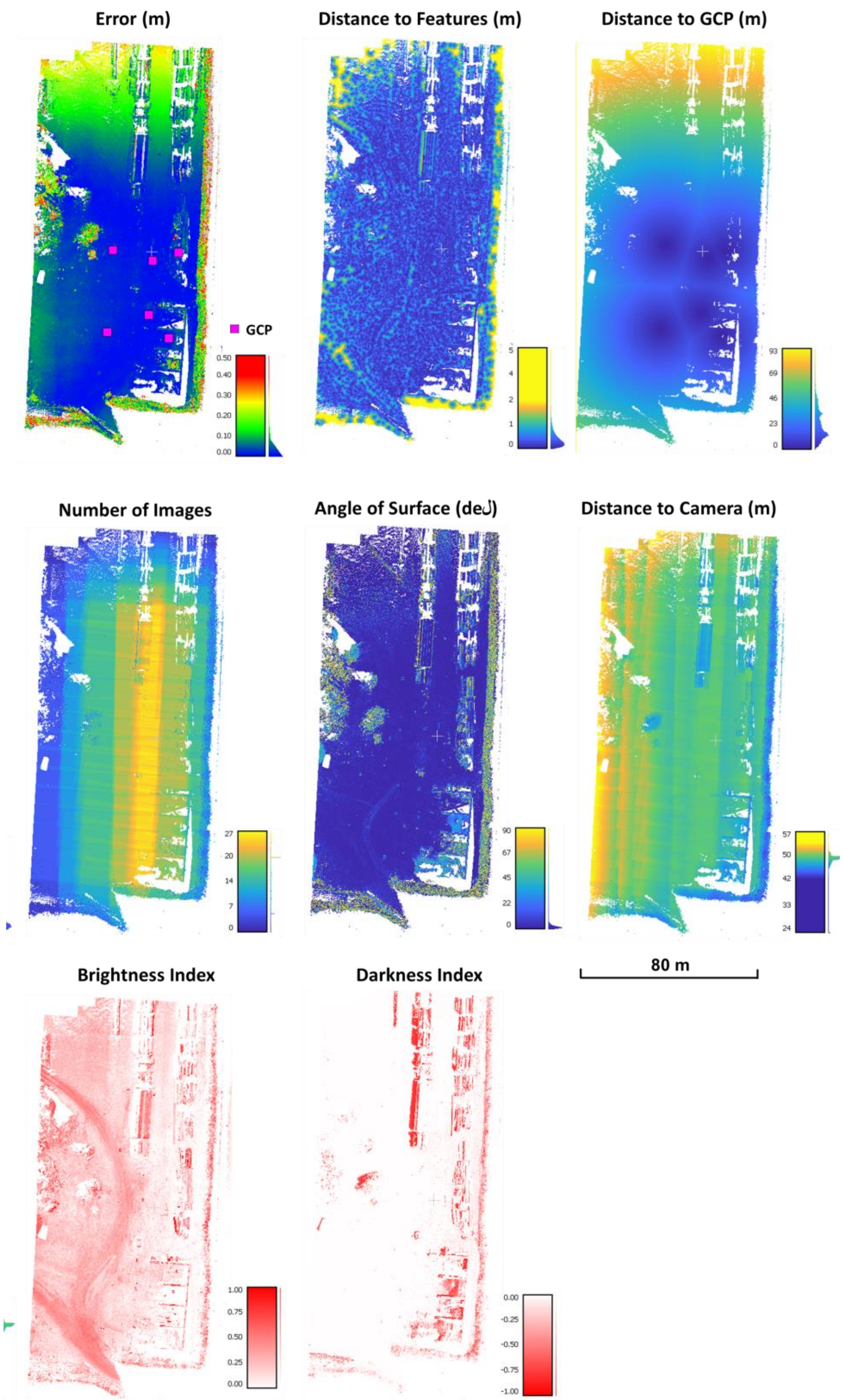

Figure 12: DPQFs for the scenario with 6 GCPs for Langmack empirical dataset

To better visualize the variations of DPQF with respect to change of lighting conditions, the simulated model and the SfM-MVS point clouds for all five scenarios of scene A are shown in Figure 13. Changing the lighting conditions from Scenario A1 to A5 impacted a number of DPQFs including, d_{kp}, I_{b} and I_{d}, as shown in Figure 13. If the ground truth point clouds are used for estimating the DPQF, there will be no variations in d_{gcp} and α_{sur}indices as they are independent form change in lighting conditions. In addition, the factors depending on the locations of cameras, i.e. d_{c} and n_{img} are minimally impacted within the simulated scenarios is this study.

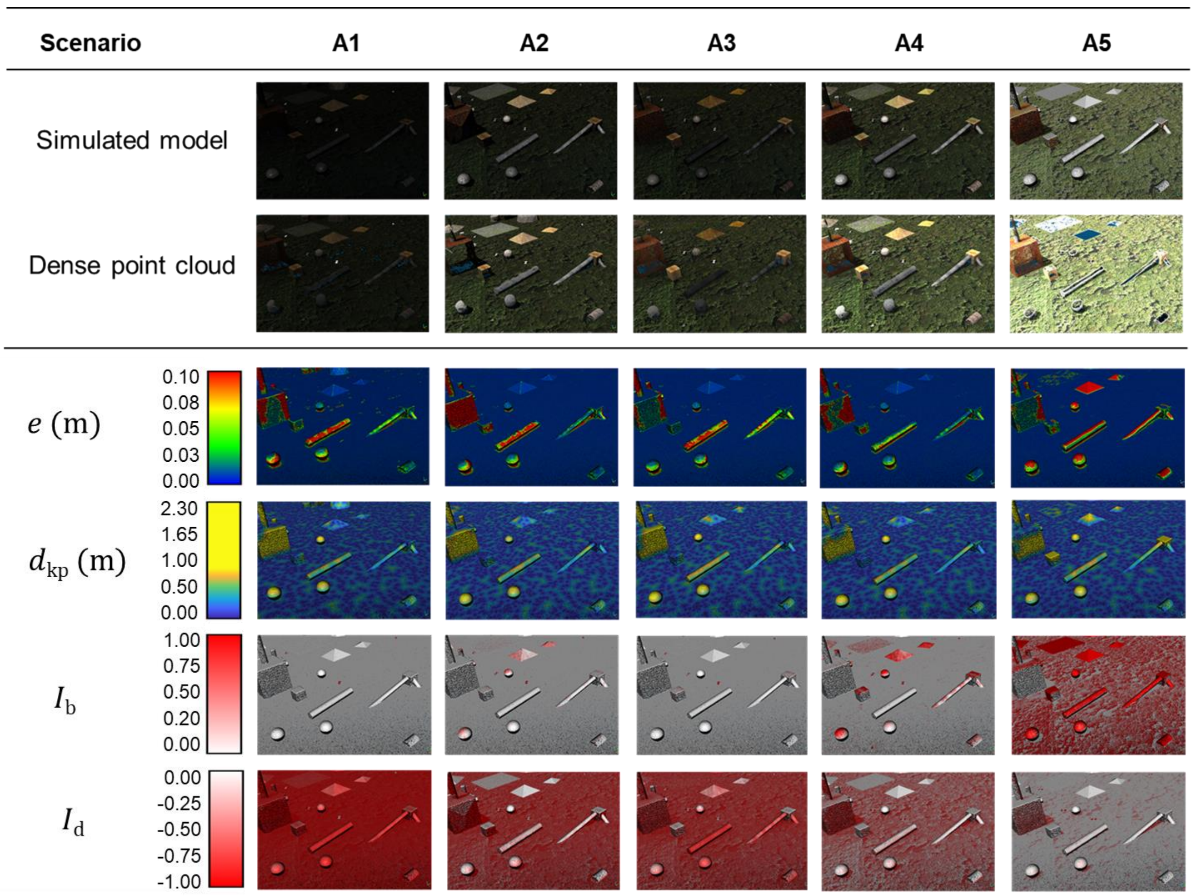

Figure 13: Change of DPQFs for scenario of simulated scene A

As shown in the Figure 13 the lighting condition had a distinguishable impact on the error in scenes. For example, as shown in 3D error visualizations, it is evident that changing the lighting conditions from scenario A1 to A2 that includes stronger shadows (lower ambient light), creates data gaps on the vertical faces. The shadow caused an error is a minimum in scenario A3, where the settings of simulation minimized the deepness of shadow by having same sun and ambient light intensity values. Increasing the sunlight intensity in simulation A5 improves the quality of reconstruction on the shadowed faces of boxes; however, at the same time, it adversely impacts the reconstruction quality on the brighter or shiny surfaces, such as the top of the pipes and the bright textured pyramids in 3D error visualizations for A5. The reason for poor reconstruction on light surfaces is that the excess of light masks features and minimizes the sparse point cloud density. Moreover, there is not enough texture to further perform matching and expanding between sparse points in densification step. As a result, data gaps and poor reconstruction occur in these overexposed regions. However, it appeared that this was not the case for areas on the flat ground surface where areas with higher brightness index still have proper 3D reconstruction from the images. This might be because of the better performance of SfM-MVS on the flat ground surface as it can be seen in both experimental and simulated datasets.

The total 3D RMSE for each simulated scenario is shown in Figure 14. It is found that both underexposed scenes (A1, A2, B1, and B2) and overexposed scenes (A5 and B5) include higher reconstruction error. This error appeared to be even higher for the overexposed situation. The scene with minimal shadow effect (A3 and B3) and the balanced sun and ambient light conditions (A4 and B4) include less error. One objective of this study is to investigate the correlations between aforementioned quality factor with the error. In addition, in order to study the relation of each factor with reconstruction error, the statistical relationships between the DPQF was calculated by developing the Pearson correlation matrices for each scenario. The correlation coefficients are between -1 and 1. The closer the coefficient is to either −1 or 1, there is a stronger dependency between the variables, and the value 0 implies that the variables are independent. The correlation coefficient matrices of the simulated scenarios are shown in Table 5. The red and blue colors indicate the positive and negative correlation, respectively, where the darker colors stand for greater correlations of each, and white color indicates no correlation between variables.

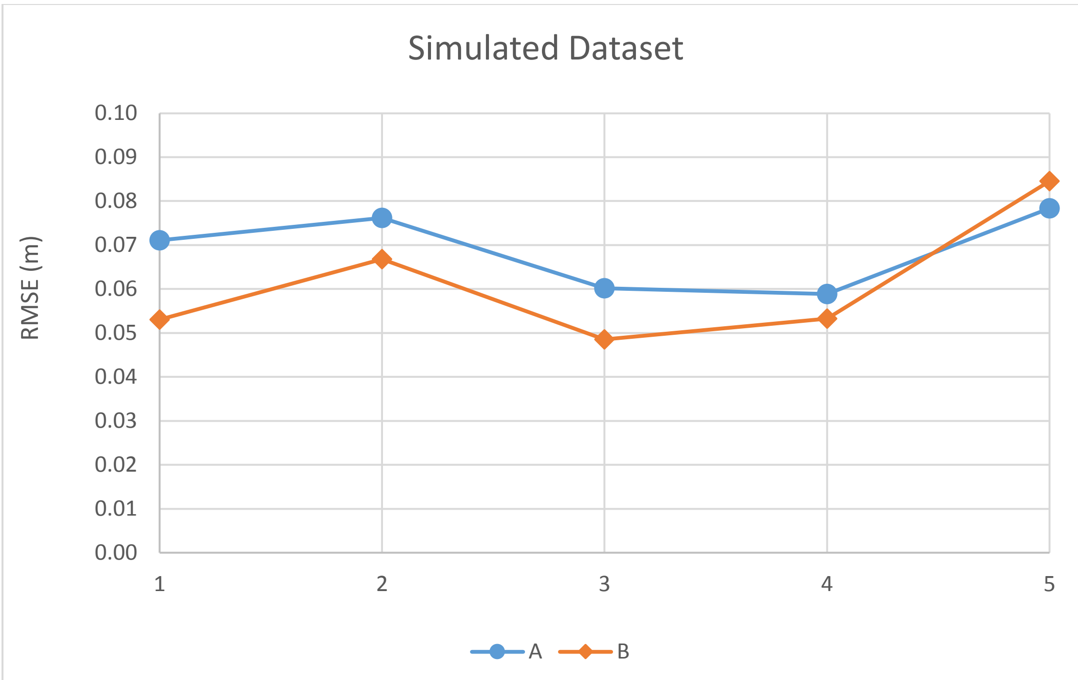

Figure 14: RMSE of 3D error for all scenarios of A and B simulations

Table 5: Pearson correlation coefficients between DPQFs for simulations A and B (matrices are symmetric).

A1	d_{kp}	d_{gcp}	d_{img}	α_{sur}	d_c	I_b	I_d
e	0.4983	-0.1219	-0.1342	0.5103	-0.1598	-0.0021	-0.1018
d_{kp}		-0.1696	-0.1882	0.6222	-0.2270	-0.0101	-0.1730
d_{gcp}			-0.6074	-0.2668	0.8898	-0.0251	0.0222
d_{img}				-0.2693	-0.5050	0.0144	0.0264
α_{sur}					-0.3490	-0.0027	-0.1516
d_c						-0.0177	0.0819
I_b							0.2958

B1	d_{kp}	d_{gcp}	d_{img}	α_{sur}	d_c	I_b	I_d
e	0.4558	-0.1186	-0.0924	0.4241	-0.1393	-0.0013	-0.1192
d_{kp}		-0.1697	-0.1314	0.5216	-0.2045	-0.0132	-0.1700
d_{gcp}			-0.6075	-0.2669	0.8898	-0.0252	0.0238
d_{img}				-0.2691	-0.5053	0.0144	0.0328
α_{sur}					-0.3489	-0.0024	-0.1754
d_c						-0.0178	0.0953
I_b							0.4037

A2	d_{kp}	d_{gcp}	d_{img}	α_{sur}	d_c	I_b	I_d
e	0.4924	-0.1351	-0.1481	0.5029	-0.1688	-0.0102	-0.1561
d_{kp}		-0.1717	-0.1881	0.6434	-0.2203	0.0065	-0.2182
d_{gcp}			-0.6074	-0.2668	0.8898	-0.0598	-0.0141
d_{img}				-0.2693	-0.5050	0.0429	0.1065
α_{sur}					-0.3490	0.0358	-0.2117
d_c						-0.0514	0.0473
I_b							0.3386

B2	d_{kp}	d_{gcp}	d_{img}	α_{sur}	d_c	I_b	I_d
e	0.4788	-0.1299	-0.1283	0.4696	-0.1590	-0.0056	-0.1751
d_{kp}		-0.1591	-0.1639	0.5689	-0.1941	0.0071	-0.2165
d_{gcp}			-0.6075	-0.2669	0.8898	-0.0861	-0.0266
d_{img}				-0.2692	-0.5053	0.0678	0.1302
α_{sur}					-0.3489	0.0506	-0.2252
d_c						-0.0862	0.0428
I_b							0.3762

A3	d_{kp}	d_{gcp}	d_{img}	α_{sur}	d_c	I_b	I_d
e	0.4498	-0.1080	-0.1006	0.4647	-0.1328	-0.0084	-0.0850
d_{kp}		-0.1957	-0.1655	0.6246	-0.2484	-0.0304	-0.1543
d_{gcp}			-0.6075	-0.2668	0.8898	0.0094	0.0989
d_{img}				-0.2691	-0.5053	-0.0167	-0.0760
α_{sur}					-0.3488	-0.0156	-0.1385
d_c						0.0258	0.1604
I_b							0.2687

B3	d_{kp}	d_{gcp}	d_{img}	α_{sur}	d_c	I_b	I_d
e	0.3814	-0.1178	-0.0605	0.3848	-0.1381	-0.0017	-0.1276
d_{kp}		-0.2194	-0.0786	0.4873	-0.2379	-0.0173	-0.0992
d_{gcp}			-0.6075	-0.2669	0.8898	-0.0205	0.1292
d_{img}				-0.2692	-0.5053	0.0122	-0.1210
α_{sur}					-0.3489	-0.0014	-0.1459
d_c						-0.0159	0.2110
I_b							0.2277

A4	d_{kp}	d_{gcp}	d_{img}	α_{sur}	d_c	I_b	I_d
e	0.4421	-0.1100	-0.1053	0.4554	-0.1277	-0.0232	-0.1810
d_{kp}		-0.1786	-0.1714	0.6210	-0.2326	-0.0407	-0.2340
d_{gcp}			-0.6075	-0.2670	0.8898	-0.0216	0.0671
d_{img}				-0.2691	-0.5053	0.0003	0.0465
α_{sur}					-0.3490	-0.0064	-0.2681
d_c						0.0202	0.1320
I_b							0.4348

B4	d_{kp}	d_{gcp}	d_{img}	α_{sur}	d_c	I_b	I_d
e	0.4298	-0.1156	-0.0770	0.4123	-0.1300	-0.0006	-0.2172
d_{kp}		-0.2080	-0.1038	0.5203	-0.2362	0.0084	-0.2261
d_{gcp}			-0.6075	-0.2669	0.8898	-0.0807	0.0875
d_{img}				-0.2692	-0.5053	0.0481	0.0324
α_{sur}					-0.3489	0.0608	-0.3153
d_c						-0.0759	0.1915
I_b							0.4323

A5	d_{kp}	d_{gcp}	d_{img}	α_{sur}	d_c	I_b	I_d
e	0.3849	-0.1034	-0.0074	0.3305	-0.1335	0.0031	-0.1341
d_{kp}		-0.1857	-0.1598	0.6148	-0.2339	-0.1083	-0.2977
d_{gcp}			-0.6074	-0.2668	0.8898	0.0697	0.1487
d_{img}				-0.2693	-0.5050	0.0358	0.0876
α_{sur}					-0.3490	-0.2444	-0.4619
d_c						0.1336	0.1926
I_b							0.5737

B5	d_{kp}	d_{gcp}	d_{img}	α_{sur}	d_c	I_b	I_d
e	0.3687	-0.0711	-0.0262	0.2565	-0.0782	0.0835	-0.1598
d_{kp}		-0.2401	-0.0783	0.5211	-0.2734	-0.0762	-0.3809
d_{gcp}			-0.6075	-0.2669	0.8898	0.0796	0.1972
d_{img}				-0.2691	-0.5053	0.0115	0.1415
α_{sur}					-0.3489	-0.2747	-0.6152
d_c						0.2027	0.2244
I_b							0.4154

Legend

It is found that in almost all A and B simulations, a higher correlation exists between error and d_{kp} and α_{sur}factors with a coefficient of 0.4 - 0.5. This correlation pattern appears to be similar in all simulations, as it can also be seen with coloring pattern of matrices in Table 5, indicating that most of the error happens near vertical surfaces or locations at a far distance from the keypoint features. The d_{kp} and α_{sur}also have higher inter-correlation, indicating that the density of sparse point cloud is lower on vertical surfaces with a high angle of incidence value. The collection between I_{d} and $\alpha_{\mathrm{sur}}$is at the highest for scenarios A5 and B5, where because of the lighting condition darker points mostly exist at the shadowed regions. Interestingly, there is a positive correlation between I_{b} and I_{d}, while these factors are supposed to negatively correlated. The reason for the correlation is because of the definition of these factors, as for most of the points the I_{b} and I_{d} are small with a normalized grayscale value close to zero. This normalized value is assigned to I_{b} and I_{d} whether the value is slightly positive or negative, and the other factor will be assigned zero value. The low values close to zero on one index and zero for the other index results is a high correlation between them. The high 0.90 correlation coefficient between d_{c} and d_{gcp} or the -0.60 between d_{gcp} and n_{img} is resulted merely because of the geometry of the scene, where all the GCPs are located at the center of the scene with more image coverage and closer distance from the cameras.

Table 6 shows the variation of the correlation coefficients of e with other DPQFs for simulations of both A and B scenes. The coefficients are comparable in most of the scenes and almost without considerable, having the high correlations between the error with d_{kp} and α_{sur}variables. This correlation coefficient will change if the simulation is adjusted by adding oblique images that capture the vertical surfaces, which are not captured in nadir images to improve the construction quality. In that case, the correlation between error and α_{sur} (or $\alpha_{inc}$for the case of oblique and nadir imagery) can decrease. Then it is possible to analyze the correlation of the other factors that are overlaid by the more significant error at a greater distance from the keypoint features at vertical surfaces.

Table 6: Changes in Pearson Correlation Coefficients of 3D error and DPQFs for all simulations of A and B.

	A1	A2	A3	A4	A5
d_{kp}	0.4983	0.4924	0.4498	0.4421	0.3849
d_{gcp}	-0.1219	-0.1351	-0.1080	-0.1100	-0.1034
d_{img}	-0.1342	-0.1481	-0.1006	-0.1053	-0.0074
α_{sur}	0.5103	0.5029	0.4647	0.4554	0.3305
d_{c}	-0.1598	-0.1688	-0.1328	-0.1277	-0.1335
I_{b}	-0.0021	-0.0102	-0.0084	-0.0232	0.0031
I_{d}	-0.1018	-0.1561	-0.0850	-0.1810	-0.1341

	B1	B2	B3	B4	B5
d_{kp}	0.4558	0.4788	0.3814	0.4298	0.3687
d_{gcp}	-0.1186	-0.1299	-0.1178	-0.1156	-0.0711
d_{img}	-0.0924	-0.1283	-0.0605	-0.0770	-0.0262
α_{sur}	0.4241	0.4696	0.3848	0.4123	0.2565
d_{c}	-0.1393	-0.1590	-0.1381	-0.1300	-0.0782
I_{b}	-0.0013	-0.0056	-0.0017	-0.0006	0.0835
I_{d}	-0.1192	-0.1751	-0.1276	-0.2172	-0.1598

Figure 15 shows the geospatial distribution of the error in SfM-MVS point clouds of the Langmack area for scenarios with different numbers of GCPs. It seems, as expected, having the appropriate number of GCPs is essential for processing the empirical dataset, and the amount of error and its distribution significantly controlled by the GCPs. For this dataset, the accuracy of 3D reconstruction considerably improves for scenarios with 8 or more GCPs. For the simulation dataset, the number of GCP did not appear to be a significant factor. This result is expected for the simulated data because the locations of cameras are known and are provided to the software, and the camera calibration model is accurately defined. However, for the empirical dataset, the impact is significant mainly because of using of an uncalibrated camera with unknown or less accurately known lens distortion parameters and low accuracy EO positions. In addition to error for scenarios with a limited number of GCPs, some points are mapped continuously as erroneous points. The point mostly belongs to the areas with high vegetation at the borders of the study area, as well as the piles of biomass located in the center. The problem with these points is that there is no well-defined surface to capture with lidar, and the lidar pulse can be from either outer or inner objects. So the ground truth lidar data for this regions is not reliable, and it is not expected to build SfM dense point cloud that reproduces the same results. In addition, there are significant errors for spaces between the concrete bridge objects, where there is no data in SfM dataset, but TLS was able to capture the geometry. The error resulted from covered objects and the error on vegetation is not meant to be included in the future analysis, so the regions with vegetation and biomass were cropped out for the final data, and the points with error larger than 21.7 cm were omitted from furthered analysis. The cut-off of 21.7 cm was decided based on the RMSE of total 3D error for cropped data of scenario with the smallest error (1.6166 × RMSE3D), also based on the performance of selected cut-off in filtering the points with an error.

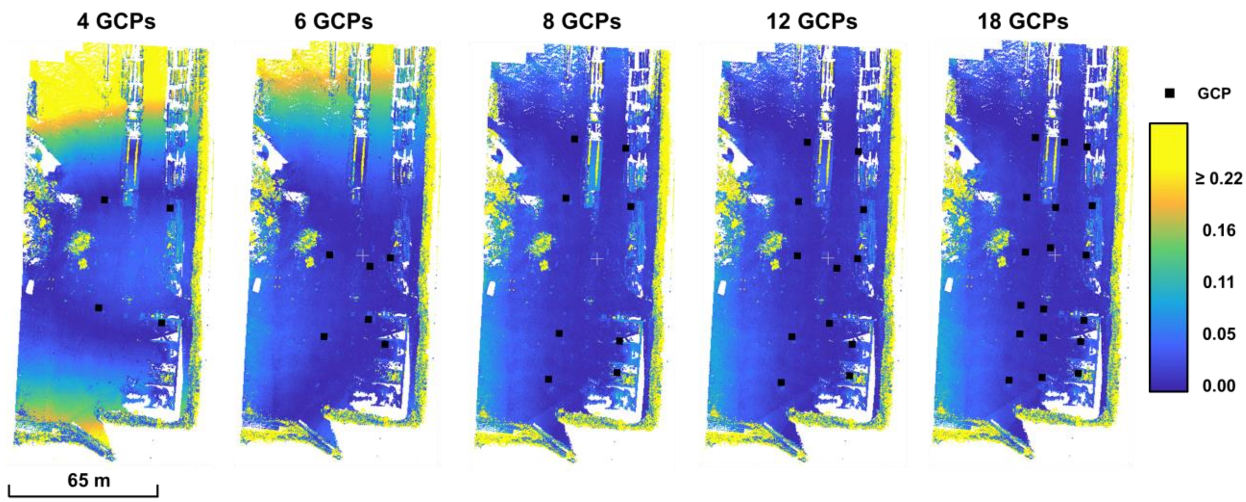

Figure 15: Changes in spatial distribution of 3D error with respect to the changes in the number of GCPs

The RMSE for cropped and filtered empirical data, the georeferencing error and the RMSE of CP error are shown in Figure 16. The error is at the highest for 4 GCPs, and it decreases as more GCPs are used for georeferencing. The trend of the change for RMSE CPs follows the same trend but with smaller values. This difference is expected because the RMSE only represents selected CP in the model that usually exist in the sparse point cloud. In most cases, the CPs are distinct objects at the scene creating key point features that can be extracted and use in sparse point clouds, which have more confident 3D construction. The regions near the high contrast markings can help to generate results that are more accurate at those locales; however, the smooth and featureless regions might have a higher error. This study shows that comparing the SfM-MVS modeled coordinates on CPs and comparing the accurately measured CPs can be a relatively good representation of overall accuracy of the sparse pointcloud; however, the higher error should be expected in dense point clouds. Interestingly, the RMSE of georeferencing increases as more GCPs are included in the processing. The reported RMSE for georeferencing error must be handled with care. This error might be because of having an error in GCP coordinates. Also, the error might increase by adding more constraints to a least square solution for coordinate transformation by providing a more realistic estimation of georeferencing error.

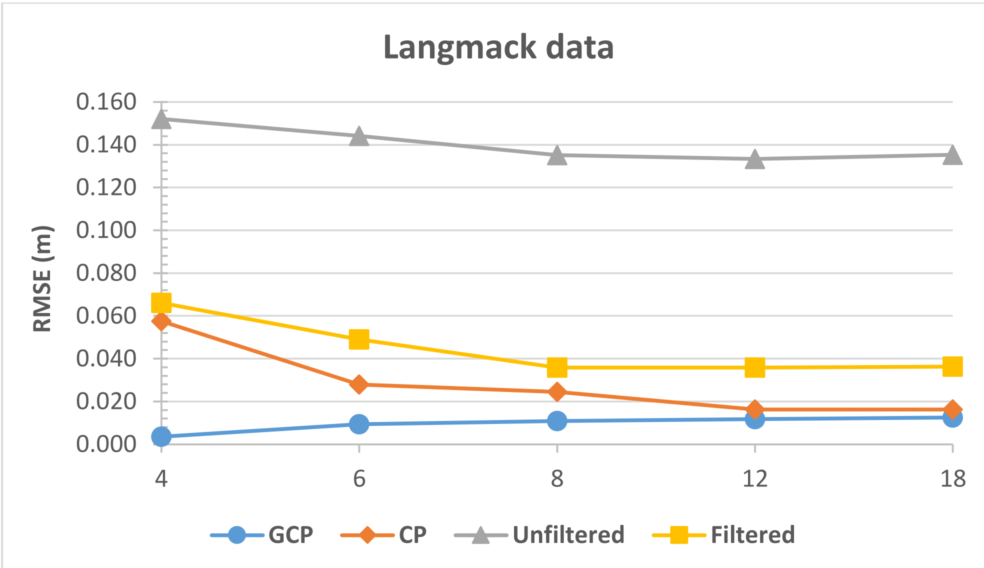

Figure 16: RMSE georeferencing error, CP error, 3D error for unfiltered and filtered data of Langmack dataset

The correlation matrices of Langmack data for scenarios with a different number of GCPs are presented in Table 7. Supporting the trend and pattern of error shown in Figure 15 and Figure 16, there is high correlation coefficient of 0.65 between e with d_{gcp} for scenarios with 4 and 6 GCPs showing that point with higher error is concurrent with areas are that located in the distance from GCPs. The results suggest that adding more GCPs significantly improves the quality of SfM result; however, the number of improvement plateaus after 8 GCPs at this site (number of GCPs is site specific and varies based on how big the site is). Also improving the accuracy by adding GCPs decreases the correlation coefficients of error and d_{gcp}. The change of correlation coefficients for e with other DPQFs are shown in Table 8. For scenarios with more GCPs, the error becomes more independent from a distance to GCP. Meanwhile, the remainder of the error shows higher correlation coefficients with n_{img}, α_{sur}, and I_{d}. The n_{img} factor is also correlated with $d_{\mathrm{gcp}}$for scenarios with 12 and 18 GCPs because more GCPs are located in the center of the area with a higher number of images. Also, the correlation between α_{sur} and d_{c} is resulted because of the site setup as the center of the study area that is closer to the cameras is flat and different objects that create α_{sur} are located around the edges of the area. However, I_{d} and α_{sur} has a meaningful correlation, while points with I_{d} values closer to -1 are located at vertical faces or overhanging surfaces that are mostly in shaded areas.

Table 7: Pearson correlation coefficients between DPQFs all scenarios of Langmack data with 4, 6, 8, 12 and 18 GCPs (matrices are symmetric).

4 GCP	d_{kp}	d_{gcp}	d_{img}	α_{sur}	d_{c}	I_{b}	I_{d}
e	0.0917	0.6525	-0.0948	0.0196	0.0849	0.0470	-0.0698
d_{kp}		0.1145	-0.2521	0.0481	0.1269	0.0422	-0.0791
d_{gcp}			-0.2995	0.0178	0.3415	0.1421	0.0499
d_{img}				-0.2772	-0.1927	-0.2076	0.0500
α_{sur}		Sym			-0.4291	0.0384	-0.4612
d_{c}						0.1702	0.2957
I_{b}							0.4111

6 GCP	d_{kp}	d_{gcp}	d_{img}	α_{sur}	d_{c}	I_{b}	I_{d}
e	0.1167	0.6458	-0.1603	0.1643	0.0430	-0.0693	-0.1845
d_{kp}		0.1113	-0.2530	0.0499	0.1178	0.0398	-0.0806
d_{gcp}			-0.2447	0.1549	0.0816	0.0884	-0.0150
d_{img}				-0.2819	-0.1741	-0.2108	0.0526
α_{sur}					-0.4284	0.0362	-0.4673
d_{c}						0.1647	0.3005
I_{b}							0.4113

8 GCP	d_{kp}	d_{gcp}	d_{img}	α_{sur}	d_{c}	I_{b}	I_{d}
e	0.1545	0.1622	-0.3302	0.3027	-0.0047	0.0465	-0.2893
d_{kp}		0.1162	-0.2578	0.0394	0.1266	0.0399	-0.0760
d_{gcp}			-0.3114	-0.1069	0.4938	0.0901	0.1434
d_{img}				-0.2788	-0.1762	-0.2100	0.0433
α_{sur}					-0.4333	0.0497	-0.4453
d_{c}						0.1590	0.2881
I_{b}							0.4040

12 GCP	d_{kp}	d_{gcp}	d_{img}	α_{sur}	d_{c}	I_{b}	I_{d}
e	0.1733	0.2879	-0.3782	0.3057	0.0881	0.0586	-0.2829
d_{kp}		0.2029	-0.2618	0.0502	0.1203	0.0377	-0.0817
d_{gcp}			-0.5186	-0.0526	0.5436	0.1659	0.1405
d_{img}				-0.2729	-0.1779	-0.2085	0.0450
α_{sur}					-0.4373	0.0460	-0.4557
d_{c}						0.1633	0.2947
I_{b}							0.4074

18 GCP	d_{kp}	d_{gcp}	d_{img}	α_{sur}	d_{c}	I_{b}	I_{d}
e	0.1762	0.3346	-0.3958	0.2863	0.1124	0.0669	-0.2747
d_{kp}		0.2180	-0.2600	0.0438	0.1242	0.0399	-0.0770
d_{gcp}			-0.6389	-0.0658	0.5205	0.1370	0.1177
d_{img}				-0.2815	-0.1742	-0.2112	0.0458
α_{sur}					-0.4333	0.0480	-0.4508
d_{c}						0.1623	0.2957
I_{b}							0.4057

Legend

-1.00 -0.75 -0.50 -0.25 0.00 0.25 0.50 0.75 1.00

Table 8: Changes in Pearson Correlation Coefficients of 3D error and DPQFs for all scenarios of Langmack data

	4 GCP	6 GCP	8 GCP	12 GCP	18 GCP
d_{kp}	0.0917	0.1167	0.1545	0.1733	0.1762
d_{gcp}	0.6525	0.6458	0.1622	0.2879	0.3346
d_{img}	-0.0948	-0.1603	-0.3302	-0.3782	-0.3958
α_{sur}	0.0196	0.1643	0.3027	0.3057	0.2863
d_c	0.0849	0.0430	-0.0047	0.0881	0.1124
I_b	0.0470	-0.0693	0.0465	0.0586	0.0669
I_d	-0.0698	-0.1845	-0.2893	-0.2829	-0.2747

4. Conclusions and future works

This paper defines quality factor indices to be used as proxy indicators for assessing the accuracy of SfM-MVS dense point clouds. The dense point cloud quality factors (DPQF) include the geometry of GCPs, the geometry of keypoint features, number of images, distance to the camera, the angle of incidence, brightness index, and darkness index. In this study, simulated and empirical experiments were used to assess the accuracy of image-based 3D reconstructed models with respect to different data collection and site conditions. The data are used to estimate the DPQF that reflect the scenarios settings, then the spatial correlation between the DPQFs and the reconstruction error to investigate for multiple datasets.

A 3D computer graphics environment was used to generate a set of simulated scenarios with different lighting conditions. Then, the virtual cameras were placed at the scene to emulate a UAS-based imagery collection and the images rendered at the defined camera locations. In addition to simulated data, real-world UAS flights were performed at a construction site to collect aerial imagery in an empirical experiment. For the empirical dataset, accurate lidar data were also collected using a terrestrial lidar scanner as a ground truth dataset. Digital images generated for simulated scenarios were post-processed using SfM-MVS techniques to produce a high-resolution

3D point cloud for each scenario. Similarly, multiple SfM datasets were processed with empirical data by adjusting the number of GCPs for georeferencing and study the results were studied.

The results were used to estimate the error and DPQF indices. The error was defined as the closeness of SfM-MVS data to the ground truth model. The ground truth geometry was precisely known for the simulated scenarios, and lidar was used as the ground truth for the empirical dataset. The result of simulated dataset demonstrated that the lighting condition had a distinguishable impact on the error *e* in scenes. In general, scenarios with stronger shadows or overexposed objects create more error. The reason is that both cases have featureless regions without visible texture, which can locally degrade the accuracy of the point clouds. The results of the experiments demonstrated that having the appropriate number of GCPs is essential for the accuracy of 3D reconstruction; however, overuse of GCPs may reach a point of diminishing return. It seems the importance of the number of GCPs for dealing with an uncalibrated camera with unknown or not accurately known EO and IO is more essential.

To compare the total RMSE, in order to study the relation of each factor with reconstruction error was compared to assess the statistical relationships between the DPQF was calculated by developing the Pearson correlation matrices for each scenario. It is found that in almost all A and B simulations, higher correlation exists between error, and the distance to the keypoint features and the angle of incidence factors with correlation pattern that appears to be similar in all simulations. The results show that the error is more significant in the areas with a lower density of sparse point cloud as well as on vertical surfaces with a high angle of incidence value. The correlation coefficients of the empirical data showed a high correlation coefficient of 0.65 between error and distance to GCP for scenarios with a smaller number of GCPS, meaning that that point with higher error is concurrent with areas are that located in a greater distance from GCPs.

However, the error becomes independent from the number of GCP. Meanwhile, the remainder of error shows higher correlation coefficients with the angle of incidence, darkness factor, and the number of images.

The paper introduced new quality factor indices for assessing the accuracy of a dense point cloud by and visualizing the error proxy indices. Definition of quality factors has tangible physical meaning that can help surveyors with planning the best data collection strategies for UAS/SfM photogrammetry. Identifying the factor during the field work can help to optimize the negative factors and minimize the SfM-MVS error that may coexist with these factors.

The result of this study shows the initial development of DPQFs with the scope of indirect accuracy assessment. More studies with more comprehensive experiments are needed to draw firm conclusions of which factor are the best for accuracy assessment in various scenarios. The advantage of the DPQFs is that the factors can be defined solely based on the inputs as results of SfM-MVS processing. The factors may provide a proxy indicator for accuracy to estimate the error estimation for dense point clouds, which is more challenging than error propagation estimation for BA procedures due to the MVS processing.

Acknowledgments

Funding for this project was provided internally by the School of Civil and Construction Engineering (CCE) at Oregon State University (OSU). The flights for empirical case study were authorized by FAA under 2016-WSA-101-COA issued to OSU. The dataset used for experimental data was also used for a conference publication for assessing the use of UAS-based photogrammetry for generating civil integrated management (CIM) models (Javadnejad et al. 2017a). We would like to thank Chase Simpson, Matthew Gillins, and Brian Weaver for their help with the field work, and Stephanie Taylor and Kevin Hamilton from Linn County Road Department, Oregon for providing access to the site. We also appreciate Leica Geosystems, David Evans and Associates, and MicroSurvey for providing surveying equipment and/or software utilized in experimental case study.

References

Abellan, A., Derron, M.-H., and Jaboyedoff, M. (2016). "'Use of 3D Point Clouds in Geohazards' Special Issue: Current Challenges and Future Trends." *Remote Sensing*, 8(2), 130.

Agisoft. (2018). "Metashape Professional v1.4." Agisoft LLC, St. Petersburg, Russia.

Agüera-Vega, F., Carvajal-Ramírez, F., and Martínez-Carricondo, P. (2017). "Accuracy of Digital Surface Models and Orthophotos Derived from Unmanned Aerial Vehicle Photogrammetry." *Journal of Surveying Engineering*, 143(2), 04016025.

Anderson, M., Motta, R., Chandrasekar, S., and Stokes, M. (1996). "Proposal for a Standard Default Color Space for the Internet—sRGB." *Color and imaging conference*, Society for Imaging Science and Technology, 238–245.

Blender. (2017). "Blender." Blender Foundation, Amsterdam, Netherlands.

Carbonneau, P. E., and Dietrich, J. T. (2017). "Cost-effective non-metric photogrammetry from consumer-grade sUAS: implications for direct georeferencing of structure from motion photogrammetry." *Earth Surface Processes and Landforms*, 42(3), 473–486.

Che, E., and Olsen, M. J. (2017). "Fast ground filtering for TLS data via Scanline Density Analysis." *ISPRS Journal of Photogrammetry and Remote Sensing*, 129, 226–240.

Clapuyt, F., Vanacker, V., and Van Oost, K. (2016). "Reproducibility of UAV-based earth topography reconstructions based on Structure-from-Motion algorithms." *Geomorphology*, 260, 4–15.

Colomina, I., and Molina, P. (2014). "Unmanned aerial systems for photogrammetry and remote sensing: A review." *ISPRS Journal of Photogrammetry and Remote Sensing*, 92, 79–97.

Crandall, D. J., Owens, A., Snavely, N., and Huttenlocher, D. P. (2013). "SfM with MRFs: Discrete-Continuous Optimization for Large-Scale Structure from Motion." *IEEE Transactions on Pattern Analysis and Machine Intelligence*, IEEE, 35(12), 2841–2853.

Dandois, J., Olano, M., and Ellis, E. (2015). "Optimal Altitude, Overlap, and Weather Conditions for Computer Vision UAV Estimates of Forest Structure." *Remote Sensing*, 7(10), 13895–13920.

Eltner, A., Kaiser, A., Castillo, C., Rock, G., Neugirg, F., and Abellán, A. (2016). "Image-based surface reconstruction in geomorphometry – merits, limits and developments." *Earth Surface Dynamics*, 4(2), 359–389.

Faraji, M. R., Qi, X., and Jensen, A. (2016). "Computer vision–based orthorectification and georeferencing of aerial image sets." *Journal of Applied Remote Sensing*, 10(3), 036027.

Fischler, M. A., and Bolles, R. C. (1981). "Random sample consensus: a paradigm for model fitting with applications to image analysis and automated cartography." *Communications of the ACM*, 24(6), 381–395.

Fonstad, M. A., Dietrich, J. T., Courville, B. C., Jensen, J. L., and Carbonneau, P. E. (2013). "Topographic structure from motion: a new development in photogrammetric measurement." *Earth Surface Processes and Landforms*, 38(4), 421–430.

Furukawa, Y., and Ponce, J. (2010). "Accurate, Dense, and Robust Multiview Stereopsis." *IEEE Transactions on Pattern Analysis and Machine Intelligence*, IEEE, 32(8), 1362–1376.

Gao, M., Xu, X., Klinger, Y., van der Woerd, J., and Tapponnier, P. (2017). "High-resolution mapping based on an Unmanned Aerial Vehicle (UAV) to capture paleoseismic offsets along the Altyn-Tagh fault, China." *Scientific Reports*, 7(1), 8281.

Girardeau-Montaut, D. (2017). "Cloud compare: 3D point cloud and mesh processing software, open-source project." *Open Source Project*, <http://www.danielgm.net/cc/> (Jan. 1, 2017).

Griffin, G. F. (2014). "The Use of Unmanned Aerial Vehicles for Disaster Management." *GEOMATICA*, 68(4), 265–281.

Harris, C., and Stephens, M. (1988). "A COMBINED CORNER AND EDGE DETECTOR." *Alvey vision conference*, 15, 50.

Harwin, S., and Lucieer, A. (2012). "Assessing the Accuracy of Georeferenced Point Clouds Produced via Multi-View Stereopsis from Unmanned Aerial Vehicle (UAV) Imagery." *Remote Sensing*, 4(12), 1573–1599.

Harwin, S., Lucieer, A., and Osborn, J. (2015). "The Impact of the Calibration Method on the Accuracy of Point Clouds Derived Using Unmanned Aerial Vehicle Multi-View Stereopsis." *Remote Sensing*, 7(9), 11933–11953.

Heung-Yeung Shum, Qifa Ke, and Zhengyou Zhang. (1999). "Efficient bundle adjustment with virtual key frames: a hierarchical approach to multi-frame structure from motion." *Proceedings. 1999 IEEE Computer Society Conference on Computer Vision and Pattern Recognition (Cat. No PR00149)*, IEEE Comput. Soc, 538–543.

Hofsetz, C., Ng, K., Chen, G., McGuinness, P., Max, N., and Liu, Y. (2004). "Image-based rendering of range data with estimated depth uncertainty." *IEEE Computer Graphics and Applications*, 24(4), 34–41.

James, M. R., Robson, S., D'Oleire-Oltmanns, S., and Niethammer, U. (2017a). "Optimising UAV topographic surveys processed with structure-from-motion: Ground control quality, quantity and bundle adjustment." *Geomorphology*, 280, 51–66.

James, M. R., Robson, S., and Smith, M. W. (2017b). "3-D uncertainty-based topographic change detection with structure-from-motion photogrammetry: precision maps for ground control and directly georeferenced surveys." *Earth Surface Processes and Landforms*, 42(12), 1769–1788.

Javadnejad, F. (2013). "Flood inundation mapping using HEC-RAS and GIS for Shelby County, Tennessee." University of Memphis.

Javadnejad, F. (2018). "Small Unmanned Aircraft Systems (UAS) for Engineering Inspections and Geospatial Mapping." Oregon State University.

Javadnejad, F., and Gillins, D. T. (2016). "Unmanned Aircraft Systems-Based Photogrammetry for Ground Movement Monitoring." *Pipelines 2016*, American Society of Civil Engineers, Reston, VA, 1000–1011.

Javadnejad, F., Simpson, C. H., Gillins, D. T., Claxton, T., and Olsen, M. J. (2017a). "An Assessment of UAS-Based Photogrammetry for Civil Integrated Management (CIM) Modeling of Pipes." *Pipelines 2017*, American Society of Civil Engineers, Reston, VA, 112–123.

Javadnejad, F., Waldron, B., and Hill, A. (2017b). "LITE Flood: Simple GIS-Based Mapping Approach for Real-Time Redelineation of Multifrequency Floods." *Natural Hazards Review*, 18(3), 04017004.

Lague, D., Brodu, N., and Leroux, J. (2013). "Accurate 3D comparison of complex topography with terrestrial laser scanner: Application to the Rangitikei canyon (N-Z)." *ISPRS Journal of Photogrammetry and Remote Sensing*, International Society for Photogrammetry and Remote Sensing, Inc. (ISPRS), 82, 10–26.

Leica Geosystems. (2016). “Cyclone v9.1.” Leica, St. Gallen, Switzerland.

LINZ. (2016). “Invercargill 0.1m Urban Aerial Photos.” *Linza Data Service*, <https://data.linz.govt.nz/layer/88147-invercargill-01m-urban-aerial-photos-2016/> (Jan. 1, 2017).

Lowe, D. G. (1999). “Object recognition from local scale-invariant features.” *Computer vision, 1999. The proceedings of the seventh IEEE international conference on*, 1150–1157.

Lowe, D. G. (2004). “Distinctive Image Features from Scale-Invariant Keypoints.” *International Journal of Computer Vision*, 60(2), 91–110.

Mahmoudabadi, H., Olsen, M. J., and Todorovic, S. (2016). “Efficient terrestrial laser scan segmentation exploiting data structure.” *ISPRS Journal of Photogrammetry and Remote Sensing*, International Society for Photogrammetry and Remote Sensing, Inc. (ISPRS), 119, 135–150.

MathWorks. (2017). “MATLAB R2017a.” Inc., MathWorks, Natick, MA.

McCaffrey, K. J. W., Jones, R. R., Holdsworth, R. E., Wilson, R. W., Clegg, P., Imber, J., Holliman, N., and Trinks, I. (2005). “Unlocking the spatial dimension: digital technologies and the future of geoscience fieldwork.” *Journal of the Geological Society*, 162(6), 927–938.

O’Banion, M. S. (2017). “Rigorous 3D Point Cloud Quality Assessment.” Oregon State University.

O’Banion, M. S., Olsen, M. J., Rault, C., Wartman, J., and Cunningham, K. (2018). “Suitability of structure from motion for rock-slope assessment.” *The Photogrammetric Record*, 33(162), 217–242.

Olsen, M., Wartman, J., McAlister, M., Mahmoudabadi, H., O’Banion, M., Dunham, L., and Cunningham, K. (2015). “To Fill or Not to Fill: Sensitivity Analysis of the Influence of

Resolution and Hole Filling on Point Cloud Surface Modeling and Individual Rockfall Event Detection." *Remote Sensing*, 7(9), 12103–12134.

Omasa, K., Hosoi, F., and Konishi, A. (2006). "3D lidar imaging for detecting and understanding plant responses and canopy structure." *Journal of Experimental Botany*, 58(4), 881–898.

OuYang, D., and Feng, H.-Y. (2005). "On the normal vector estimation for point cloud data from smooth surfaces." *Computer-Aided Design*, 37(10), 1071–1079.

Pajares, G. (2015). "Overview and Current Status of Remote Sensing Applications Based on Unmanned Aerial Vehicles (UAVs)." *Photogrammetric Engineering & Remote Sensing*, 81(4), 281–330.

Pix4D. (2018). "Pix4Dmapper Pro v4.0." Pix4D, Lausanne, Switzerland.

Remondino, F., Spera, M. G., Nocerino, E., Menna, F., and Nex, F. (2014). "State of the art in high density image matching." *The Photogrammetric Record*, 29(146), 144–166.

Seitz, S. M., Curless, B., Diebel, J., Scharstein, D., and Szeliski, R. (2006). "A Comparison and Evaluation of Multi-View Stereo Reconstruction Algorithms." *2006 IEEE Computer Society Conference on Computer Vision and Pattern Recognition - Volume 1 (CVPR'06)*, IEEE, 519–528.

Shi, Y., Thomasson, J. A., Murray, S. C., Pugh, N. A., Rooney, W. L., Shafian, S., Rajan, N., Rouze, G., Morgan, C. L. S., Neely, H. L., Rana, A., Bagavathiannan, M. V., Henrickson, J., Bowden, E., Valasek, J., Olsenholler, J., Bishop, M. P., Sheridan, R., Putman, E. B., Popescu, S., Burks, T., Cope, D., Ibrahim, A., McCutchen, B. F., Baltensperger, D. D., Avant, R. V., Vidrine, M., and Yang, C. (2016). "Unmanned Aerial Vehicles for High-Throughput Phenotyping and Agronomic Research." *PLOS ONE*, (J. Zhang, ed.), 11(7), e0159781.

Slocum, R. K., and Parrish, C. E. (2017). "Simulated Imagery Rendering Workflow for UAS-

Based Photogrammetric 3D Reconstruction Accuracy Assessments.” *Remote Sensing*, 9(4), 396.

Smith, M. W., and Vericat, D. (2015). “From experimental plots to experimental landscapes: topography, erosion and deposition in sub-humid badlands from Structure-from-Motion photogrammetry.” *Earth Surface Processes and Landforms*, 40(12), 1656–1671.

Snavely, N., Seitz, S. M., and Szeliski, R. (2006). “Photo tourism.” *ACM SIGGRAPH 2006 Papers on - SIGGRAPH ’06*, ACM Press, New York, New York, USA, 835.

Snavely, N., Seitz, S. M., and Szeliski, R. (2008). “Modeling the World from Internet Photo Collections.” *International Journal of Computer Vision*, 80(2), 189–210.

Sohn, G., and Dowman, I. (2007). “Data fusion of high-resolution satellite imagery and LiDAR data for automatic building extraction.” *ISPRS Journal of Photogrammetry and Remote Sensing*, 62(1), 43–63.

Szeliski, R. (2010). *Computer Vision: Algorithms and Applications*. Springer-Verlag New York, Inc., New York, NY, USA.

Tomasi, C., and Kanade, T. (1992). “Shape and motion from image streams under orthography: a factorization method.” *International Journal of Computer Vision*, 9(2), 137–154.

Tonkin, T., and Midgley, N. (2016). “Ground-Control Networks for Image Based Surface Reconstruction: An Investigation of Optimum Survey Designs Using UAV Derived Imagery and Structure-from-Motion Photogrammetry.” *Remote Sensing*, 8(9), 786.

Triggs, B., McLauchlan, P. F., Hartley, R. I., and Fitzgibbon, A. W. (1999). “Bundle adjustment—a modern synthesis.” *International workshop on vision algorithms*, 298–372.

Westoby, M. J., Brasington, J., Glasser, N. F., Hambrey, M. J., and Reynolds, J. M. (2012). “‘Structure-from-Motion’ photogrammetry: A low-cost, effective tool for geoscience applications." *Geomorphology*, 179, 300–314.

Wood, R. L., Gillins, D. T., Mohammadi, M. E., Javadnejad, F., Tahami, H., Gillins, M. N., and Liao, Y. (2017). "2015 Gorkha Post-Earthquake Reconnaissance of a Historic Village with Micro Unmanned Aerial Systems." *16th World Conference on Earthquake (16WCEE),* International Association for Earthquake Engineering (IAEE).

Wu, C. (2011). "VisualSFM: A Visual Structure from Motion System."

Yao, Y., Zhu, H., Nie, Y., Ji, X., and Cao, X. (2014). "Revised depth map estimation for multi-view stereo." *2014 International Conference on 3D Imaging (IC3D),* IEEE, 1–7.

Zhu, Z., Stamatopoulos, C., and Fraser, C. S. (2015). "Accurate and occlusion-robust multi-view stereo." *ISPRS Journal of Photogrammetry and Remote Sensing*, 109, 47–61.